CORTEX 153 (2022) 235–256

Available online at www.sciencedirect.com

ScienceDirect

Journal homepage: www.elsevier.com/locate/cortex

Special Issue "Brain and cognitive asymmetry in clinical disorders": Research Report

# The inferior frontal sulcus: Cortical segregation, molecular architecture and function

Sabine H. Ruland [a,*], Nicola Palomero-Gallagher [a,b,c], Felix Hoffstaedter [d,e], Simon B. Eickhoff [d,e], Hartmut Mohlberg [a] and Katrin Amunts [a,b]

[a] Institute of Neuroscience and Medicine (INM-1), Research Centre Jülich, Jülich, Germany
[b] C. & O. Vogt Institute for Brain Research, University Hospital Düsseldorf, Heinrich-Heine University Düsseldorf, Düsseldorf, Germany
[c] Department of Psychiatry, Psychotherapy and Psychosomatics, Medical Faculty, RWTH Aachen University, Aachen, Germany
[d] Institute of Neuroscience and Medicine (INM-7), Research Centre Jülich, Jülich, Germany
[e] Institute of Systems Neuroscience, Medical Faculty, Heinrich Heine University Düsseldorf, Düsseldorf, Germany

ARTICLE INFO

*Article history:*
Received 19 October 2021
Reviewed 1 December 2021
Revised 10 March 2022
Accepted 18 March 2022
Published online 19 April 2022

*Keywords:*
Inferior frontal sulcus
Inferior frontal junction
Cytoarchitecture
Receptor autoradiography
Coordinate-based meta-analysis

ABSTRACT

The inferior frontal sulcus is conceptualized as the landmark delineating ventro-from dorsolateral prefrontal cortex. Functional imaging studies report activations within the sulcus during tasks addressing cognitive control and verbal working memory, while their microstructural correlates are not well defined. Existing microstructural maps, e.g., Brodmann's map, do not distinguish separate areas within the sulcus. We identified six new areas in the inferior frontal sulcus and its junction to the precentral sulcus, *ifs1-4*, *ifj1-ifj2*, by combined cytoarchitectonic analysis and receptor autoradiography. A hierarchical cluster analysis of receptor densities of these and neighbouring prefrontal areas revealed that they form a distinct cluster within the prefrontal cortex. Major interhemispheric differences were found in both cyto- and receptor-architecture. The function of cytoarchitectonically identified areas was explored by comparing probabilistic maps of the areas in stereotaxic space with their functions and co-activation patterns as analysed by means of a coordinate-based meta-analysis. We found a bilateral involvement in working memory, as well as a lateralization of different language-related processes to the left hemisphere, and of music processing and attention to the right-hemispheric areas. Particularly *ifj2* might act as a functional hub between the networks. The cytoarchitectonic maps and receptor densities provide a powerful tool to further elucidate the function of these areas. The maps are available through the Human Brain Atlas of the Human Brain Project and serve in combination with the information on the cyto- and receptor architecture of the areas as a resource for brain models and simulations.



* *Corresponding author*. Research Centre Jülich, Wilhelm-Johnen-Strasse, 52428, Jülich, Germany.
E-mail address: s.ruland@fz-juelich.de (S.H. Ruland).

https://doi.org/10.1016/j.cortex.2022.03.019

## 1. Introduction

The microstructural organization of the inferior frontal sulcus (IFS) received little attention in the past as compared to neighbouring areas of the dorso-lateral and ventrolateral cortices. Brodmann's map does not show distinct areas within the sulcus (Brodmann, 1909), but indicates area 9 dorsally to the IFS, areas 45 and 44 ventrally, and area 46 occupying both the middle and inferior frontal gyrus. In functional imaging studies the IFS is considered as the macroscopic landmark separating Broca's region (Broca, 1861) involved in speech processing (Friederici & Gierhan, 2013) from the mid-dorsolateral prefrontal cortex associated with cognitive control in working memory (Petrides, 2000). Recent studies show that also tertiary sulci of the prefrontal cortex which occur late in development and show a high variability in their patterns consist of functional distinct components (Miller et al., 2021a, 2021b). However, due to the lack of three-dimensional maps, activations within the IFS are often attributed to either the middle or inferior frontal.

Interestingly, functional imaging studies investigating verbal working memory or cognitive control reported distinct activations within the inferior frontal sulcus and its junction with the inferior precentral sulcus (preCS) (Brass & von Cramon, 2002; Makuuchi et al., 2009). The latter region has been called the inferior frontal junction (IFJ) area, and has been specifically associated with brain functions during task switching, more precisely the updating of task goals (Derrfuss et al., 2004). More recent studies have shown that the cortex of the IFS is specific for implementing versus memorizing verbal instructions (Demanet et al., 2016) and that the IFJ is involved in attention shift (Tamber-Rosenau et al., 2018; Zhang et al., 2018).

Research on the architecture of multiple receptors of neurotransmitters of our own group has suggested that the IFS and IFJ is occupied by several areas, which differ in their receptor pattern from those of neighbouring areas of Broca's region (Amunts et al., 2010). It is plausible to assume that differences in the receptor densities and pattern of multiple receptors between cortical areas in this region correlate with a specific functional role. Multimodal mapping based on combined cytoarchitectonics and quantitative in-vitro receptor autoradiography of different receptor types and neurotransmitter systems became a powerful tool to define structurally, but also functionally relevant parcellations of the cerebral cortex (Amunts & Zilles, 2015).

The aim of this study was therefore to map the IFS and IFJ using a multimodal approach based on receptor- and cytoarchitecture, to compute probabilistic maps of the delineated areas in standard stereotaxic space, to integrate the maps of the areas into the broader context of Julich-Brain, https://jubrain.humanbrainproject.eu (Amunts et al., 2020), and finally, to explore the functions and connectivity of the cytoarchitectonically defined areas using the BrainMap database (Laird et al., 2011), within the same reference space. The BrainMap database collects the results of thousands of neuroimaging findings for functional decoding and allows the assessment of task-based functional connectivity through the analysis of co-activation patterns (Eickhoff et al., 2009) based on the Anatomy Toolbox (Eickhoff et al., 2005).

## 2. Materials and methods

We report how we determined our sample size, all data exclusions, all inclusion/exclusion criteria, whether inclusion/exclusion criteria were established prior to data analysis, all manipulations, and all measures in the study. No part of the study procedures or analyses was preregistered prior to the research being conducted.

### 2.1. *Cyto- and receptorarchitectonic mapping*

Analysis was performed in two different samples. Sample 1 was stained for cell bodies, the second was receptor autoradiographic processed.

In sample 1, ten human post mortem brains (5 male, 5 female, age 68 ± 14 years) were used for cytoarchitectonic analysis. Brains were obtained through the body donor program of the Department of Anatomy at the University of Düsseldorf, Germany. Subjects had no indications of neurologic or psychiatric diseases and the post mortem delay was between 12 and 24 h. Histological processing has been published by Amunts et al. (2020). Brains were fixed in formalin or in a Bodian mixture, embedded in paraffin and sectioned in 6000–7500 20 μm thick coronal slices. Every 15th section was mounted on a gelatine-covered glass slide and stained for cell bodies using a modified silver staining (Merker, 1983). Regions of interest (ROIs) were defined in those sections which contained the inferior frontal sulcus (IFS) and/or the inferior precentral sulcus (preCS). The IFS and preCS were identified according to Ono et al. (1990). Each ROI was scanned automatically with a resolution of 1.02 μm/pixel using an Axiovision (Zeiss, Germany) connected to a microscope (Axioplan 2 imaging, Zeiss, Germany) and a CCD-Camera (Axiocam MRm, Zeiss, Germany). Grey level index (GLI) images were determined by inhouse MatLab scripts for Windows (MatLab R2009a; Mathworks Inc., Natick, MA, USA). The GLI is a measure of the volume fraction of cell bodies in a field of 16 × 16 pixel in the scanned ROI (Schleicher & Zilles, 1990), and has a strong correlation with cell packing density values.

For receptor autoradiographic processing in sample 2, seven human hemispheres (4 male, 3 female, age 77 ± 2 years) were obtained in accordance to the guidelines of the local ethical committee through the body donor program of the Department of Anatomy at the University of Düsseldorf, Germany. The post mortem delay was between 12 and 18 h. None of the patients had a record of neurological or psychiatric diseases. After autopsy the hemispheres were split into 2–3 cm thick coronal slabs, frozen in isopentane at −40 °C and stored at −80 °C. Slabs were serially cut into 20 μm thick sections using a large-scale cryostat microtome. Alternating glass-mounted sections were processed for receptor autoradiography or stained for visualization of cell bodies (Palomero-Gallagher et al., 2008). Seventeen receptors of the glutamatergic (AMPA, kainate, NMDA, mGlu2/3 receptors), GABAergic ($GABA_A$, $GABA_B$ receptors, BZ binding sites), cholinergic (muscarinic $M_1$, $M_2$, $M_3$, nicotinic $\alpha_4/\beta_2$ receptors), adrenergic ($\alpha_1$, $\alpha_2$ receptors), serotonergic ($5\text{-}HT_{1A}$, $5\text{-}HT_2$ receptors), dopaminergic ($D_1$ receptors), and adenosinergic ($A_1$ receptors) transmitter systems were studied. Distance

between autoradiographs of the same receptor was approximately 1.4 mm. The labeling procedure has been published previously (Zilles, Schleicher, et al., 2002; Zilles, Palomero-Gallagher, et al., 2002). In short, the protocol consisted of a preincubation, a main incubation and a rinsing step. During the preincubation, the tissue was rehydrated and endogenous substances which block binding sites for the tritiated ligand (AMPA receptor - $^3$H-AMPA ligand, kainate - kainate, NMDA - MK-801, mGlu2/3 - LY 341495, $GABA_A$ - Muscimol, $GABA_B$ - CGP 54626, BZ - Flumazenil, $M_1$ - Pirezepin, $M_2$ - Oxotremorin-M, $M_3$ - 4-DAMP, nicotinic $\alpha1/\beta2$ - Epibatidin, $\alpha_1$ - Prazosin, $\alpha_2$ - UK 14.304, 5-$HT_{1A}$- 8-OH-DPAT, 5-$HT_2$ - Ketanserin, $D_1$ - SCH-23390, $A_1$ - CPFPX) were washed out. In the main incubation, sections were incubated in a buffer solution including the tritiated ligand or the tritiated ligand and an unlabeled specific displacer. The incubation with a displacer is necessary to detect nonspecific binding. Non-specific binding was less than 5% of the total binding in all cases. Finally, the rinsing step stopped the binding process, eliminated unbounded tritiated ligands and buffer salts. After the labeling procedure, the radioactively marked sections and plastic standards with known reactivity concentrations (Microscales, Amersham) were coexposed to tritium-sensitive films (Hyperfilm, Amersham) for 4–18 weeks depending on the actual ligand. The transformation of the grey values in the autoradiographs to receptor densities was described by Zilles, Palomero-Gallagher, et al. (2002). First, the autoradiographs were digitalized using an Axiovision image analyzing system (Zeiss, Germany) connected to a CCD-camera with a resolution of 2600 × 2060 pixels. A calibration curve computed with the grey values of the plastic standards specified the exponentially decreasing relationship between grey values and radioactivity concentrations. The concentration of radioactivity (R) was converted to receptor density in fmol/mg protein ($C_b$) by means of the following equation:

$$C_b = \frac{R}{E \times B \times W_b \times S_a} \times \frac{K_D + L}{L} \times 10^{12}$$

where E is the efficiency of the scintillation counter (amount of radioactivity in the incubation buffer), B the number of decays per unit of time and radioactivity, $W_b$ the protein weight of a standard, $S_a$ the specific activity of the ligand, $K_D$ the dissociation constant of the ligand, and L the free concentration of ligand during incubation. Finally, the grey value of each pixel in the resulting linearized image coded for a receptor density in fmol/mg protein. For visualization of regional and laminar distribution patterns, the linearized images were smoothed, contrast enhanced and colour coded.

Areal borders were detected in cell body stained and receptor autoradiographically labeled sections using image analysis and multivariate statistics. The procedure for localization of cortical borders is based on the fact that cortical areas differ in their laminar distribution pattern of receptor densities (in receptor autoradiographs) or in their laminar cell packing density (in cell body stained slices). To characterize laminar distribution patterns and cell packing densities, profiles were extracted from the linearized images and GLI images using in-house programmed applications of MatLab for Windows (MatLab R2009a; Mathworks Inc., Natick, MA, USA). First, two contour lines were defined. For receptor autoradiography, the outer contour was set at the pial surface and the inner contour was traced along the layer VI/white matter border. In GLI images, the outer contour was set at the layer I/layer II border and the inner contour at the layer VI/white matter border. These two lines were used as start and endpoints of vertically orientated traverses along which density profiles were extracted (Schleicher et al., 2000). Profile shape was quantified by extracting a feature vector with ten elements based on central moments (mean density, mean x, standard deviation, skewness, kurtosis and their derivatives) from each profile. Differences between feature vectors, which indicate differences in profile shape, were quantified using the Mahalanobis Distance. To increase the signal-to-noise-ratio, averaged feature vectors of two adjacent blocks of profiles, ranging from 8 to 18 profiles per block in receptor autoradiography and from 10 to 24 profiles per block in the GLI images, were calculated. Mahalanobis distance functions were established by calculating the distances between all pairs of neighbouring cortical blocks and plotting the values as a function of the profile position. Maxima of the Mahalanobis distances revealed the most dissimilar laminar pattern, i.e., a border between areas. The significance ($p < .01$) of these maxima was assessed by a Hotelling $T^2$-test and a Bonferroni correction. In summary, significant maxima of the Mahalanobis distance between blocks of density profiles indicated locations of cortical borders.

Mean (averaged over all cortical layers) and laminar receptor densities of all 17 receptors as well as laminar cell packing densities of the mapped areas were calculated using mean density profiles. In addition to the newly detected areas, the receptor and cell packing densities of the neighbouring areas were measured. Three Regions of Interest (ROIs) for each area located on 3 consecutive sections were chosen which were free of artefacts and showed a perpendicular orientation of the sectioning plane to the cortical surface. A block of 11 adjacent density profiles in the receptor autoradiographs and 15 profiles in the GLI image were extracted from each ROI and averaged to one mean receptor density and one mean GLI density profile. The area below the receptor density profile of a given receptor quantifies the laminar receptor density in fmol/mg protein from the pial surface to the layer VI/white matter border for that specific receptor. In accordance, the given GLI profile quantifies the laminar cell packing density from the layer I/-layer II border to the layer VI/white matter border of that area. Mean areal receptor densities were calculated by averaging the values over the whole cortical ribbon (i.e., over all cortical layers). Laminar densities were extracted from mean profiles by computing the surface of discrete segments defined by the borders between layers. Each segment represented a cortical layer and its relative width. For receptor autoradiographs, the layers were defined on the corresponding cell body stained section.

Furthermore, inter-hemispheric differences of laminar cell and receptor densities of the newly mapped areas were analysed using the same statistical model as for the observer-independent border definition. Instead of an ANOVA which would be not indicative because of the small sample size of three left and four right autoradiographically processed hemispheres, the Mahalanobis distances were calculated between all left and right density profiles of each area and tested for significance by a permutation test ($p < .05$ and a Bonferroni

correction) using house programmed applications of MatLab for Windows (MatLab R2009a; Mathworks Inc., Natick, MA, USA).

The hierarchical cluster analysis was conducted to visualize putative groupings of areas according to the degree of (dis)similarity of their receptor architecture. The mean receptor densities have been normalized to assign equal weight to each receptor. The hierarchical cluster classified areas into groups or clusters in such a way that areas in the same cluster are similar with respect to their receptor architecture, and different from areas in other clusters using the MatLab Statistics Toolbox (MatLab R2009a; Mathworks Inc., Natick, MA, USA). We applied the Euclidean distance as a measure of (dis) similarity and the Ward linkage algorithm as the linkage method (Palomero-Gallagher et al., 2009), since they yielded the maximum cophenetic coefficient, which quantifies how well the dendrogram represents the multi-dimensional distances within input data. In addition, we determined the number of stabile clusters by a subsequent k-means analysis and the elbow approach (Rousseeuw, 1987).

### 2.2. 3D reconstruction and probability maps

The ten cytoarchitectonically analysed brains and mapped areas within the IFS and preCS were 3D reconstructed (Amunts et al., 2020) using three data sets of each brain: (i) the structural MRI data set of the fixed brain, (ii) the photo data set of blockfaces recorded during sectioning, and (iii) the data set of high-resolution flatbed scans of the cell body stained sections, on which the detected areal borders were transferred using the in-house software *sectiontracer*. Both linear and nonlinear transformations were applied to correct for deformations during histological processing. The reconstructed brains and areas were warped to the MNI (Montreal Neurological Institute) reference brain (Evans et al., 1993) by linear and nonlinear elastic transformations. Coordinates were brought into the anatomical MNI space by shifting the data 4 mm caudally on the y-axis and 5 mm dorsally on the z-axis (Amunts et al., 2005). Areas mapped in the ten brains were superimposed separately to generate a probability map for each area (Amunts et al., 2020). Each voxel indicates the frequency an area occurs in the reference brain. Values ranging from 10% to 100% (10% means that an area is located in this voxel in only one brain) were coded by a heat map with colours from blue (10%) to red (100%).

Furthermore, a maximum probability map (MPM) of each area was calculated (Amunts et al., 2020; Eickhoff et al., 2006). Therefore, the probabilities in each voxel of all areas were compared so that a voxel was assigned to the area which showed the highest probability in it. Voxels with identical probabilities were assigned to the area with the highest averaged probability of the neighbouring voxels. Border regions where neighbouring areas are not yet mapped were 40% thresholded.

Volumes of the cytoarchitectonically defined areas were determined for each hemisphere of the ten brains. The calculation was based on the areal surface (in voxels) marked on the digitized cell body stained sections, the thickness and distance between these sections. Furthermore, the shrinking factor of each brain corrected the areal volumes for histological processing. It was determined as a ratio between the fresh volumes and the volumes after fixation (Amunts et al., 2005).

Monte Carlo permutation tests ($p < .05$; Bonferroni corrected for multiple comparisons) were carried out to analyse inter-hemispheric and gender differences of areal volumes using the MatLab Statistics Toolbox (MatLab R2009a; Mathworks Inc., Natick, MA, USA). Thereby, areal volumes were presented as a fraction of whole-brain volume to correct for differences in total brain sizes.

The details of this approach are described by Amunts et al. (2020). There was no new analysis code developed for this study.

### 2.3. Meta-analytic connectivity modeling and behavioral domains

A whole-brain coordinate-based meta-analysis was carried out to detect brain regions co-activated with the newly mapped areas in functional neuroimaging experiments included in the BrainMap database, www.brainmap.org (Eickhoff et al., 2009; Fox & Lancaster, 2002; Laird et al., 2009, 2011). Only fMRI and PET experiments from healthy subjects were used (approximately 8000 studies). Areas were represented by their maximum probability maps (MPMs) which were used as seed regions. All experiments with an activation in the seed region were identified (left *ifs1/2* 188 experiments, right *ifs1/2* 66, left *ifs3* 212, right *ifs3* 85, left *ifs4* 193, right *ifs4* 64, left *ifj1* 560, right *ifj1* 340, left *ifj2* 470, right *ifj2* 482) and tested for convergence across all foci reported in these experiments. Each focus was modulated as a center of 3D Gaussian probability distribution by the activation likelihood estimation (ALE) due to the spatial uncertainty of the neuroimaging results (Eickhoff et al., 2012). The ALE co-activation maps were thresholded at a cluster-level FWE corrected $p < .05$ (cluster-forming threshold at voxel level $p < .001$). Localization of clusters was characterized using the SPM Anatomy Toolbox (Eickhoff et al., 2005). Furthermore, each experiment in the BrainMap database was assigned to a behavioral domain (Laird et al., 2009). Significantly ($p < .05$, Bonferroni corrected for multiple comparisons) over-represented behavioral domains of experiments activating the seed regions decoded the functions of the newly mapped areas.

## 3. Results

Six new cortical areas within the IFS (*ifs1*-*ifs4*), and the IFJ (*ifj1*, *ifj2*) were identified and mapped over their whole extent in a total of 27 hemispheres of 14 human postmortem brains. The study encompassed two different samples – sample 1 for in-depth analysis of the cytoarchitecture, and the subsequent calculation of probabilistic maps of the areas based on serial, cell-body stained sections of 10 brains, and sample 2 for receptorarchitectonic analysis to study the concentration and regional distribution of receptors of different neurotransmitters (7 hemispheres of 4 brains).

The new cortical areas were analysed in coronal sections by differences in the size and distribution of cell bodies, and packing densities across the cortical layers (=cytoarchitecture)

as well as by laminar and regional differences in the receptor concentrations of different receptor types (=receptor architecture). Seventeen receptors of the glutamatergic (AMPA, kainate, NMDA, mGlu2/3 receptors), GABAergic ($GABA_A$, $GABA_B$ receptors, BZ binding sites), cholinergic (muscarinic $M_1$, $M_2$, $M_3$, nicotinic $\alpha_4/\beta_2$ receptors), adrenergic ($\alpha_1$, $\alpha_2$ receptors), serotonergic ($5\text{-}HT_{1A}$, $5\text{-}HT_2$ receptors), dopaminergic ($D_1$ receptors), and adenosinergic ($A_1$ receptors) transmitter systems were studied to characterize the molecular architecture of this region, and to verify and strengthen cytoarchitectonic mapping by a multimodal approach. The localization of cyto- and receptor architectonic borders was based on an observer-independent method and statistical criteria for defining significant differences between neighbouring areas in receptor architecture (Schleicher et al., 2000).

### 3.1. *Cyto- and receptor architecture of the IFS and IFJ*

Six new cortical areas within the IFS (*ifs1-ifs4*), and the IFJ (*ifj1*, *ifj2)* were cytoarchitectonically and receptor architectonically mapped.

The new areas shared some common characteristics, which made them distinct from neighbouring cortices (Fig. 1A), but also expressed specific features, which allowed us to separate them from each other. Characteristic common cytoarchitectonic features of areas *ifs1*, *ifs2*, *ifs3*, *ifs4, ifj1,* and *ifj2* (Fig. 2) include a barely recognizable layer IV invaded by pyramidal cells of layers III and V, which associated these areas with the dysgranular cortical type. In addition, these areas had a blurred layer II/III border, and a subdivision of layer III into an upper part with smaller and a lower part with larger pyramidal cells. Layer V also showed a gradient in pyramidal cell size from large cells in the upper and smaller ones in lower V, with a low cell density. The more specific cytoarchitectonic features of each of the areas were as follows: area *ifs3* differed from the other areas by very large pyramidal cells in the broad, lower part of layer III, and a clear columnar arrangement of cells throughout all layers. Area *ifs2* showed a thinner lower part of layer III with smaller pyramidal cells, a thinner and less dense layer IV, and a less distinct layer VI than the other *ifs* and *ifj* areas. Area *ifs4* had a densely packed layer VI, a clear subdivision of layer V due to the existence of larger, more densely packed pyramids in its upper half, and a less striking subdivision of layer III. Area *ifs1* showed a similar subdivision of layer III as *ifs3*, but much smaller and less densely packed pyramidal cells as well as a less pronounced layer V/VI border due to smaller cells in layer VI. Areas *ifj1* and *ifj2* were both characterized by a blurred transition between layer VI and the white matter, densely packed granular cells in layer II as well as large pyramidal cells mainly in deep layer III. Area *ifj2* contained a higher number of large pyramidal cells in upper layer V and large pyramidal cells almost exclusively in the very low part of layer III, as compared to *ifj1*. Cytoarchitectonic features are also summarized in S1 Table.

Areas *ifs1*, *ifs2*, *ifs3*, *ifs4, ifj1,* and *ifj2* also differed between each other and with respect to neighbouring areas (Fig. 1B) in their receptor architecture. The receptor types showed characteristic laminar patterns (Fig. 3). Whereas the glutamatergic kainate receptors, for example, reached their highest densities in layers V-VI, the $GABA_A$ receptors were most dense in layer III. The distinction between the different cortical areas was based on lower or higher receptor densities in similar layers, while maintaining the same general laminar distribution pattern of the given receptor. Area *ifs2* showed, in contrast to the other mapped areas, the lowest densities of $GABA_A$ and $\alpha_1$ receptors in layers V-VI, of serotonergic $5\text{-}HT_{1A}$ and $5\text{-}HT_2$ receptors in layers II-V, and of nicotinic $\alpha_4/\beta_2$ receptors throughout the cortex. Area *ifs3* had the highest densities of kainate receptors in layers IV-VI, of mGlu2/3 receptors densities in III-V, of BZ binding sites in II-IV. Area *ifs4* presented the highest densities of AMPA and adrenergic $\alpha_2$ receptors in layers I-III, of $M_2$ receptors over all layers, of nicotinic $\alpha_4/\beta_2$ receptors in layers I–V, and of $5\text{-}HT_2$ receptors in layer III. The most striking receptor architectonic characteristics of *ifs1* were the very low $A_1$ receptor densities for adenosin in layers I-III and the highest $D_1$ receptor densities in layers II-V. Area *ifj1* was characterized by the lowest concentrations of kainate receptors over all layers and of NMDA receptors in layers I-IV. Finally, *ifj2* stood out by the lowest densities of $GABA_A$ receptors in layers V-VI and of $M_2$ receptors in layers III-VI, as well as by the highest ones of AMPA receptors in layers II-III, of $5\text{-}HT_{1A}$ receptors in all layers, and of $GABA_B$ receptors in layers I-III. Receptor architectonic features are also summarized in S1 Table.

To investigate inter-hemispheric differences, the receptor and cell densities of *ifs1*-4, *ifj1* and *ifj2* of the left and right hemispheres were compared based on a multivariate distance measure: Mahalanobis distances were calculated between receptor and cell density profiles of each area of left and right hemispheres. 88 out of possible 96 distances were significant, while only eight did not reach significance (permutation test, $p < .05$, Bonferroni correction). The most pronounced differences were detected for $5\text{-}HT_{1A}$, BZ, kainate, $M_3$, and $GABA_A$ receptor densities, where receptors densities were higher concentrated in the right hemisphere. Area *ifs2* showed very large areal left-right differences as indicated by highest distance values (S1 Fig). The $5\text{-}HT_{1A}$ density for example was in *ifs2* of the right hemisphere 88% higher as in the left-hemispheric *ifs2*.

A hierarchical cluster analysis of the mean receptor densities (mean densities of a receptor averaged over the cortical layers of an area) of the new identified areas and neighbouring regions revealed areal groupings depending on their receptor architectonic similarities (Fig. 4). Mean densities of *ifs1* (DOI: https://www.doi.org/10.25493/SHG2-7RS), *ifs2* (DOI: https://www.doi.org/10.25493/14M7-QJR), *ifs3* (DOI: https://www.doi.org/10.25493/Z5JN-J28), *ifs4* (DOI: https://www.doi.org/10.25493/YF9R-J87), *ifj1* (DOI: https://www.doi.org/10.25493/JS85-VQD), and *ifj2* (DOI: https://www.doi.org/10.25493/VN1A-Q2R) are also available on EBRAINS. Interestingly, areas of the IFJ were more similar to each other than to one of the *ifs* areas. Furthermore, *ifs1 and 2* were more similar to each other than to *ifs3 and ifs 1/2* and 3 are more similar to each other than to *ifs4*. Areas in the IFS and IFJ were distinct from those of the Broca's region (areas 44v, 44d and 45a, 45p, Amunts et al., 2010), but share more similarities than with the mid-DLPFC Brodmann areas 46, 9 as described in Rajkowska et al. (Rajkowska & Goldman-Rakic, 1995a, 1995b) and the premotor cortex (area 6).

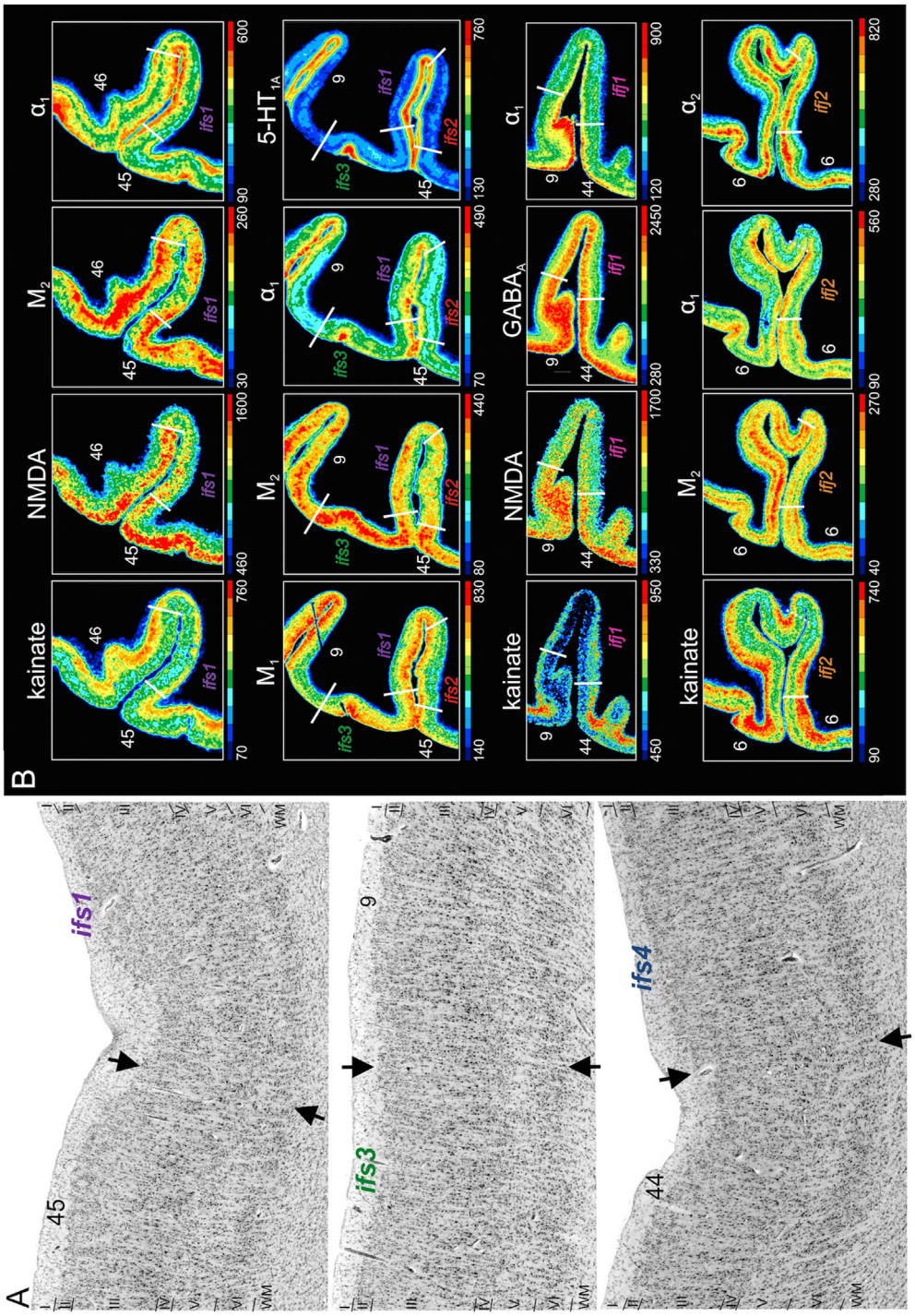


**Fig. 1 – Cytoarchitectonic and receptor architectonic borders of areas *ifs1*-*ifs4*, *ifj1*, and *ifj2*. (A) Cytoarchitectonic borders (black arrows) of areas *ifs1*-*ifs4*, *ifj1*, and *ifj2* between 45/*ifs1*, *ifs3* and dorsally adjacent BA9 at posterior middle frontal gyrus (not yet mapped), and 44/*ifs4*. Roman numerals (I-VI) indicate cortical layers. The neighbouring areas on the inferior (Geyer et al., 1996, 1999) and middle frontal gyrus (Derrfuss et al., 2004; Zilles & Amunts, 2009) show a broader and more conspicuous layer IV, a higher number of larger pyramidal cells in lower layer III, a clear columnar arrangement of the cells throughout all layers as well as a more densely packed and broader VI. (B) Receptor architectonic borders (white lines) between 45/*ifs1* and *ifs1*/46 were characterized by lower kainate, NMDA, $M_2$, and $\alpha_1$ receptor densities in *ifs1*. Area *ifs2* was differentiated from *ifs1* and 45 by lower and *ifs3* from *ifs1* and pMFG by higher $M_1$, $M_2$, $\alpha_1$ and $5\text{-}HT_{1A}$ receptor densities. Borders between 44/*ifj1* and *ifj1*/9 were defined by lower kainate, NMDA, $GABA_A$, and $\alpha_1$ receptor densities in *ifj1*. The *ifj2*/6 border was identified by higher concentrations of the four shown receptors in 6. Colour bars indicate receptor densities in fmol/mg protein. Cyto- and receptor architectonical borders were all confirmed by the observer-independent method (Schleicher et al., 2000). WM, white matter.**

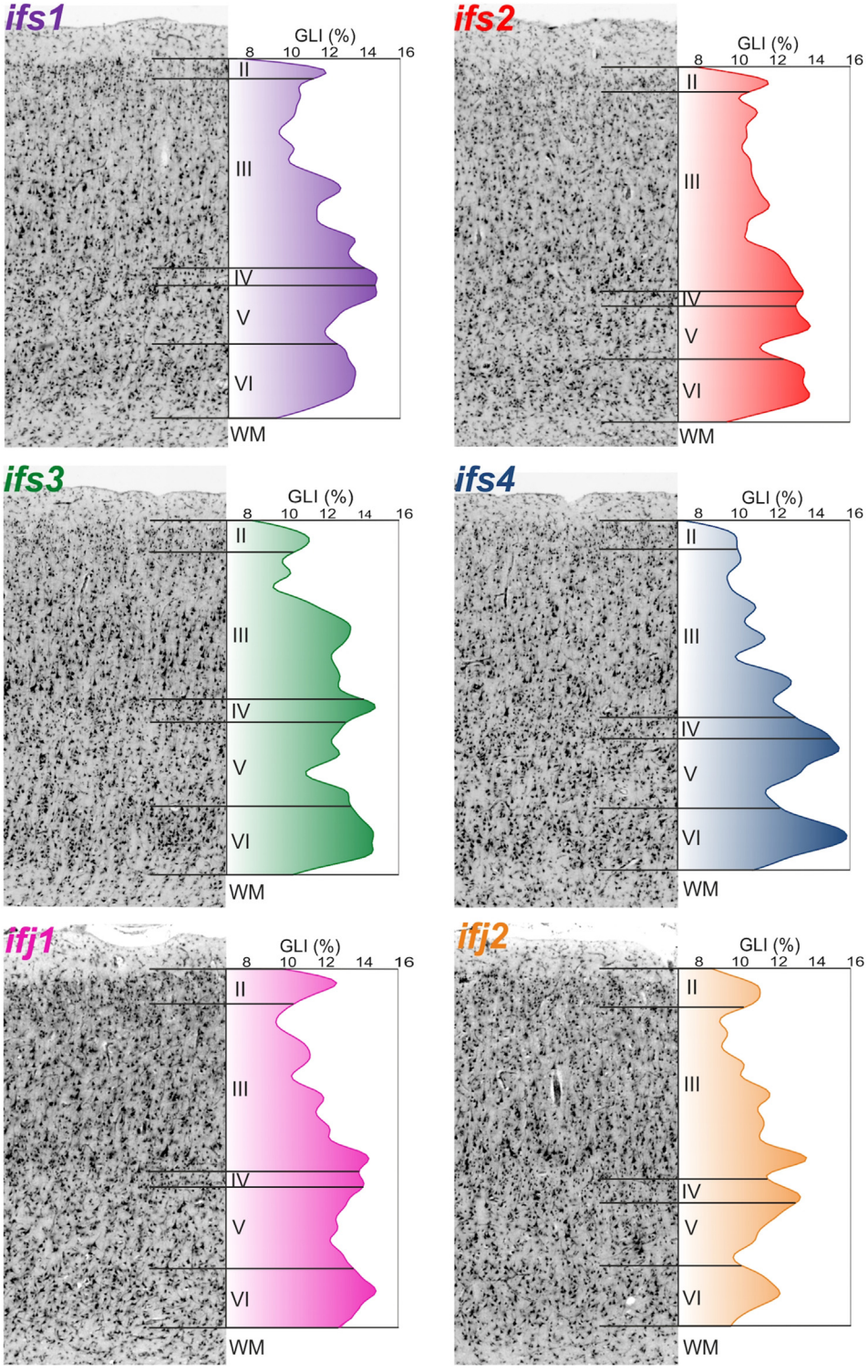


**Fig. 2 – Cytoarchitecture of areas *ifs1*-*ifs4*, *ifj1*, and *ifj2*. Photomicrographs of coronal, cell body stained sections through each area, and the corresponding cell density (GLI) profiles. Roman numerals (I-VI) indicate cortical layers. Areas differ mainly by size of layer III pyramidal cells (pc) and the relative thickness of its upper (small and medium size pc) and lower part (large size pc), the cell packing density and borders of layer VI as well as the distribution of large pc in V. WM, white matter.**

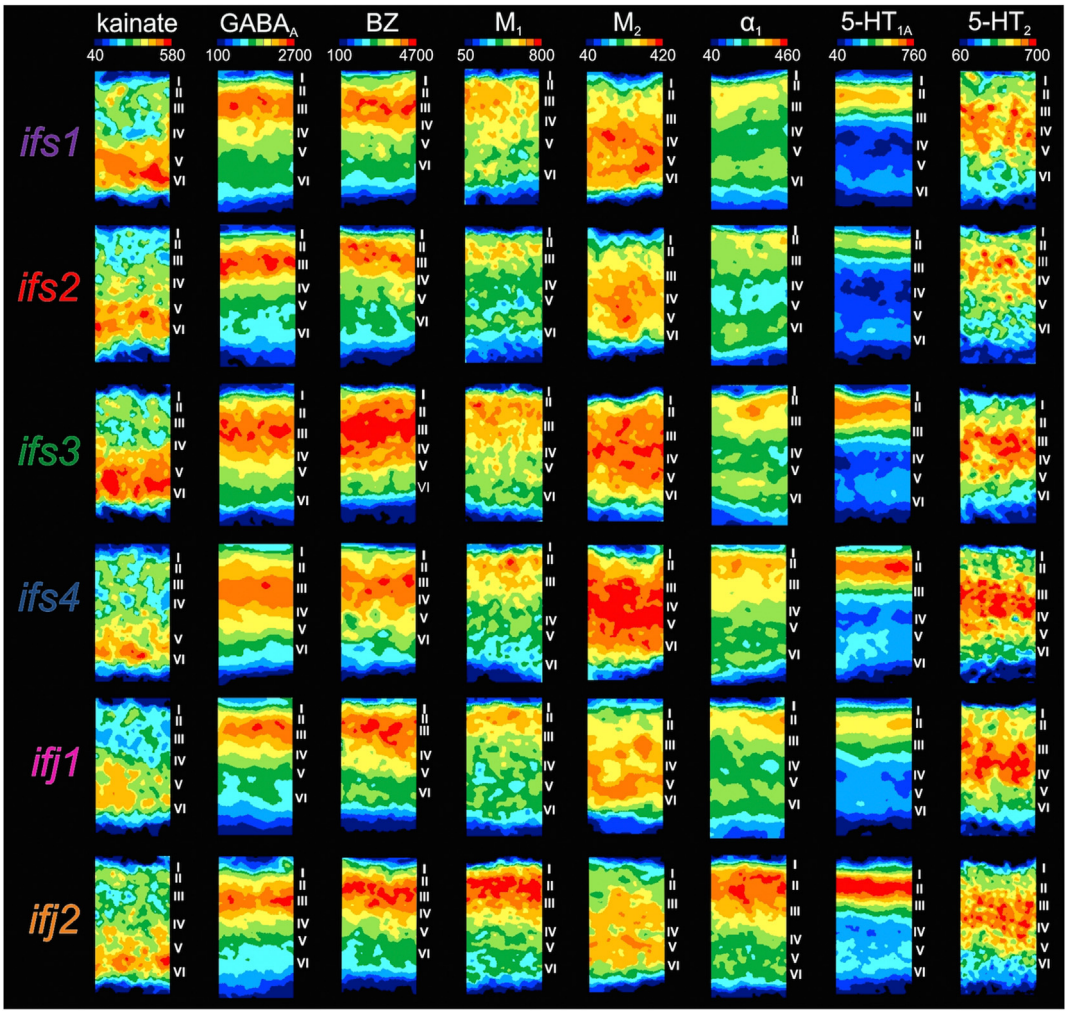


**Fig. 3 – Receptor architecture of areas *ifs1-ifs4*, *ifj1*, and *ifj2*. Colour coded receptor autoradiograms of 8 of the 17 examined receptors of coronal sections. Colour bars indicate receptor densities (in fmol/mg protein) from black for low to red for high receptor densities. Roman numerals (I-VI) mark the positions of the cortical layers. The areas differ by lower or higher receptor densities in same layers, while maintaining the same general laminar distribution pattern of the given receptor. For example, *ifs3* stand out by the highest BZ receptor densities in layers II and III, and of the kainate receptors in layers V/VI. Highest $M_2$ receptor concentrations are seen in III-VI of *ifs4*. Very low densities of the $GABA_A$ and $\alpha_1$ receptors are measured in layers V-VI of *ifs2* and those of the 5-$HT_{1A}$ receptors in II-V. Area *ifj2* is characterized by high concentrations of the $GABA_A$ receptors in V/VI, $M_2$ receptors in III-VI, and 5-$HT_{1A}$ over all layers. Colour coded autoradiograms of *ifs1* (DOI: https://www.doi.org/10.25493/SHG2-7RS), *ifs2* (DOI: https://www.doi.org/10.25493/14M7-QJR), *ifs3* (DOI: https://www.doi.org/10.25493/Z5JN-J28), *ifs4* (DOI: https://www.doi.org/10.25493/YF9R-J87), *ifj1* (DOI: https://www.doi.org/10.25493/JS85-VQD), and *ifj2* (DOI: https://www.doi.org/10.25493/VN1A-Q2R) are also available on EBRAINS.**

### 3.2. *Localisation and probabilistic maps in 3D space*

Areas *ifs1*-*ifs4* were arranged in a rostro-caudal and ventro-dorsal order within the IFS (Figs. 5–7). Area *ifs1*, the most rostral area, was found on the ventral and dorsal banks of the IFS. Areas *ifs2* and *ifs4* were detected exclusively on the ventral bank, whereas *ifs3* was found on the dorsal one, and sometimes encroached onto the free surface of the middle frontal gyrus. Areas *ifs1* and *ifs2* were delimited ventrally by area 45, the anterior part of Broca's region. Area 44, the posterior part of Broca's region, was located ventral to *ifs4*. Additionally, *ifs1* was followed dorsally by 46, whereas *ifs3* abutted 9. Areas *ifj1* and *ifj2* were located within the IFJ. Area *ifj1* extended on the ventral bank of the IFS, whereas *ifj2* was detected caudally to *ifj1* with an extension in the part of the inferior precentral sulcus mainly ventrally, but also caudally to the junction. Areas *ifj1* and *ifj2* were delimited ventrally by area 44 and dorsally by 9. Finally, *ifj2* shared a border with area 6, which was located on the precentral gyrus.

The location of *ifs* and *ifj* areas was highly determined by the inter-individual sulcal patterns of the IFS, preCS and their junction (Fig. 5). If the IFS was interrupted into two segments and did not have a long connection to the preCS, *ifs* and *ifj* areas were separated by a gyri. Then, the *ifs* areas were located in the anterior segment and the *ifj* areas were located in the shorter posterior segment of the IFS and the preCS (see Fig. 5 B1L and

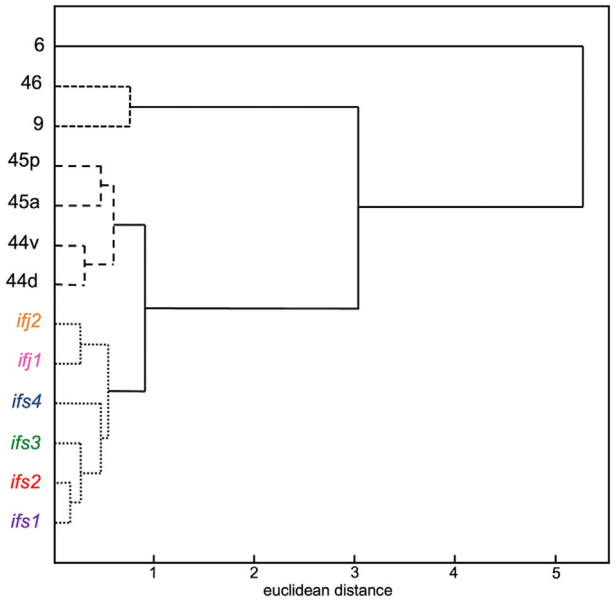


**Fig. 4 – Hierarchical cluster analysis of areas within the IFS and IFJ as well as their neighbouring regions, Broca's region (areas 45a, 45p, 44d, 44v), the mid-DLPFC (Brodmann areas 46, 9) and Brodmann area 6, based on the mean densities of 15 receptors. Areas in the same cluster are similar with respect to their receptor architecture, and different from areas in other clusters. The analysis reveals 4 clusters: First the ifs and ifj areas, second the areas of Broca's region, third the areas of the mid-DLPFC and fourth area 6 (indicated by differently dotted lines). Areas *ifs1* and *ifs2* are more similar to each other than to *ifs3* and *ifs4* and the *ifs* areas share more similarities than with *ifj1* and *ifj2*. Finally, the *ifs* and *ifj* areas are more similar to the areas of Broca's region than to the areas of the mid-DLPFC and area 6. (cophenetic coefficient = .98). In addition, the number of stabile clusters by a subsequent k-means analysis and the elbow approach supported the 4 clusters of the hierarchical cluster analysis.**

B3L). This case occurred in 3 left hemispheres of the ten cytoarchitectonically mapped brains (incidence rate: right hemisphere 0%, left hemisphere 30%). In some cases, area *ifs3* reached partially small parts of the middle frontal gyrus. This occurred in three of the mapped brains bilaterally in the left and right hemisphere (incidence rate: 30%). This seems to be determined by the depth and further sulcus-internal foldings of the IFS. If the IFS is not that deep and not folded internally, *ifs3* reached the middle frontal gyrus (see Fig. 5).

An interpolated map of areas *ifs1* (DOI: https://www.doi.org/10.25493/YM3R-9SP), *ifs2* (DOI: https://www.doi.org/10.25493/6RNA-WG4), *ifs3* (DOI: https://www.doi.org/10.25493/RNQP-F5U), *ifs4* (DOI: https://www.doi.org/10.25493/GX3R-2ET), *ifj1* (DOI: https://www.doi.org/10.25493/18S5-89W), and *ifj2* (DOI: https://www.doi.org/10.25493/Z6GM-61X) in one of the 10 individual cytoarchitectonic mapped brains (not shown in Fig. 5), the BigBrain (Amunts et al., 2013), is accessible on EBRAINS and can be viewed in the interactive atlas viewer and is also available through the BigBrain portal at https://bigbrainproject.org/hiball.html).

Probabilistic maps (pmaps) were generated to quantify the inter-individual variability in extent and localization of the areas (Fig. 6). The areas identified in sample 1 were transformed to the stereotaxic MNI-Colin27 and ICBM2009casym reference space and superimposed (Amunts et al., 2020). The overlap of areas in this space was colour coded. The pmaps of areas *ifs1* (DOI: https://www.doi.org/10.25493/HNZP-56M), *ifs2* (DOI: https://www.doi.org/10.25493/NJD4-CM4), *ifs3* (DOI: https://www.doi.org/10.25493/DGGC-X7Q), *ifs4* (DOI: https://www.doi.org/10.25493/P3QK-2V6), *ifj1* (DOI: https://www.doi.org/10.25493/V9PK-H82), and *ifj2* (DOI: https://www.doi.org/10.25493/1WG8-WBE) are part of the Julich-Brain, https://jubrain.humanbrainproject.eu (Amunts et al., 2020) can be viewed in the interactive atlas on EBRAINS. The areas show a high inter-individual variability. The portions with a low probability of 10–50% cover a large part of the overall pmaps volume. In addition, the pmaps of *ifj1*, *ifs4* and *ifs2* showed only a small portion with an overlap of the individual maps of 100%. Areas *ifs1-4*, *ifj1* and *ifj2* had also different volumes - the smallest area was *ifs2*, with an average volume of 38 $mm^3$ (±19 $mm^3$; ±SD), followed by *ifs4* with 115 $mm^3$ (±53 $mm^3$), *ifs1* with 177 $mm^3$ (±74 $mm^3$) and *ifj1* with 193 $mm^3$ (±81 $mm^3$). Largest volumes were detected for *ifs3* with 224 $mm^3$ (±107 $mm^3$) and *ifj2* with 260 $mm^3$ (±149 $mm^3$). A permutation test of the areal volumes indicated that there were no significant inter-hemispheric or gender differences ($p > .05$). Table 1 shows the coordinates of the centre of gravity of the pmaps of *ifs1-ifs4*, *ifj1* and *ifj2*.

To reduce complexity and to visualize the extent of areas, we then computed maximum probability maps (MPMs) of areas *ifs1-4*, *ifj1* and *ifj2* (Fig. 7), assigning each voxel to the most likely histological area at that position (Eickhoff et al., 2005). The MPMs of the areas can not reflect all anatomical details of the areas in the individual brains, but they provide a solid basis for the localisation of activations in neuroimaging studies.

### 3.3. *Functional decoding and co-activation patterns*

In order to provide first insights in the function of the areas, a quantitative functional decoding of areas *ifs1-4*, *ifj1* and *ifj2* was performed. Whole-brain co-activation profiles, i.e., task-based functional connectivity, were analysed using the BrainMap database www.brainmap.org (Fox & Lancaster, 2002). Because of the very small size and high inter-individual variability of *ifs2*, the probability in none of the voxels of greater size used for the MPM calculated for the functional decoding could be assigned to *ifs2* because its probability was higher than those of neighbouring areas. Therefore, we calculated a combined MPM of *ifs2* and *ifs1* taking into account their structural similarities revealed by the hierarchical cluster. Taking the MPMs of areas *ifs1/2*, *ifs3*, *ifs4*, *ifj1* and *ifj2* as seed regions, we first filtered the database for all experiments showing activations within the respective region. Behavioral domains (Eickhoff et al., 2009) significantly associated with areas *ifs1/2*, *ifs3*, *ifs4*, *ifj1* and *ifj2* are illustrated in Fig. 8. In summary, *ifs* and *ifj* areas of the left hemisphere were associated with language-related and working memory processes, whereas their right hemispheric correlates were involved in music processing, working memory, and attention

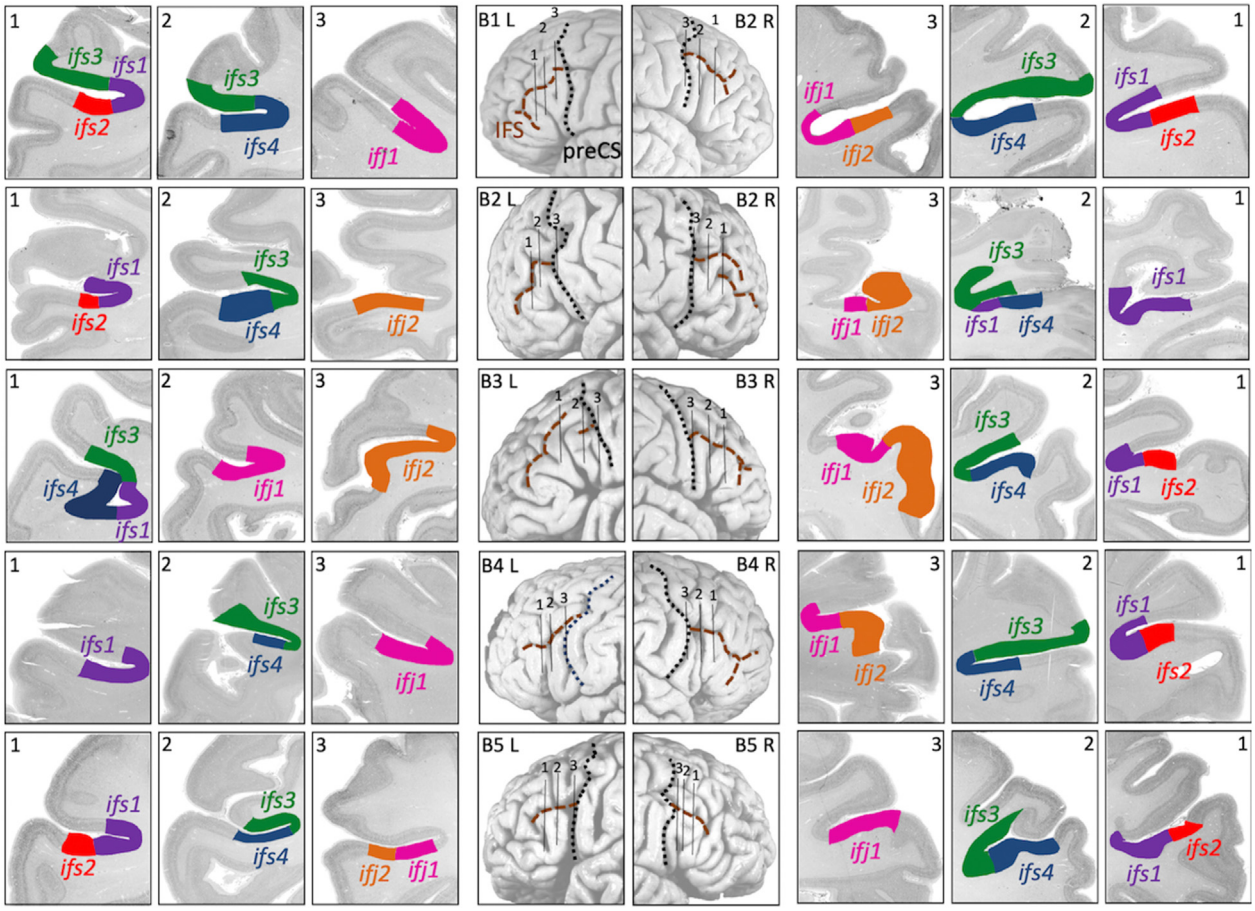


**Fig. 5 – Inter-individual variability of the IFS, IFJ and the *ifs* and *ifj* areas. Columns 4 and 5 show photographs of the lateral surfaces of the left (L) and right (R) hemispheres of 5 post mortem brains (B1–B5). The IFS and the preCS are marked with dotted lines to show examples of the inter-individual variability of the sulcal patterns of the IFS and preCS as well as their junction. Sulcal patterns according to the terminology of Ono et al. (1990): B1 L: IFS interrupted; true, short connection of IFS and preCS, R: IFS continuous; true, long connection of IFS and preCS. B2 L: IFS continuous, true, long connection of IFS and preCS, R: IFS interrupted; true, short connection of IFS and preCS. B3 L: IFS interrupted; true, short connection of IFS and preCS, R: IFS continuous; true, long connection of IFS and preCS. B4 L: IFS continuous, true, long connection of IFS and preCS, R: IFS continuous; true, long connection of IFS and preCS. B5 L: IFS continuous, true, long connection of IFS and preCS, R: IFS continuous; true, long connection of IFS and preCS. Columns 1–3 and 6–8 show cutouts from sections and mapped areas in these sections. Locations of sections are marked with numbers (1-3) in photographs of the brain surfaces.**

processing. Right *ifs3* showed no behavioral domains significantly associated with, but the uncorrected data revealed an involvement of this area in working memory and attention.

Functional connectivity analysis revealed numerous brain regions common co-activated with *ifs1/2, ifs3, ifs4, ifj1* and *ifj2* (Fig. 9, Table 2). Both conjunctions (separately conjunction analyses for the left and right hemisphere) revealed bilateral clusters in the IFG, IFS, IFJ, preCG, MFG, FOP, IL, putamen, thalamus, SMA, aMCC, pMCC, IPG, IPS, SPG, FG as well as in the right MOG, right cerebellum, left postCG, and left IOG. In addition, left *ifs* and *ifj* areas were common co-activated with left LOG, right AG, right ITG, left SOG, and left MOG. Right *ifs1-4, ifj1*, and *ifj2* showed co-activations in bilateral thalamus, SMG, POP, left MFG, left MTG left STG, right MOG, and right SOG. Differences between co-activation patterns of the delineated areas were shown by their specific co-activations, brain regions significantly more co-activated with the considered area than with the others (Fig. 9, Table 2). Areas *ifs1/2*, *ifs3*, and *ifs4* were not significantly more co-activated with any brain region than *ifj1* or *ifj2* did. Therefore, and due to their structural similarity revealed by the cluster analysis (Fig. 4) their MPMs were combined to a seed region including all *ifs* areas (*ifs1-4*). Specific co-activations of left *ifj2* were found bilaterally in the IFJ, IFG, preCG, pMCC, SMA, putamen, thalamus, cerebellum, IPG, SMG, left postCG, left FOP, left IPS, left IOG and left MFG. Left *ifj1* was specifically co-activated with the left IFJ, left IFG, left and right SMA, and right IFS. Left *ifs1-4* was specifically co-activated with clusters located on left and right IFS, left IFG, left LOG, left IPS, left AG, left ITG and MTG. Right hemispheric *ifj2* was specifically co-activated with bilateral IFG, preCG, FOP, insular lobe, pMCC, SMA, putamen, SMG, POP, SPG, MOG, left IOG, left precuneus, left ITG, left thalamus, right IPS and right IPG. Specific

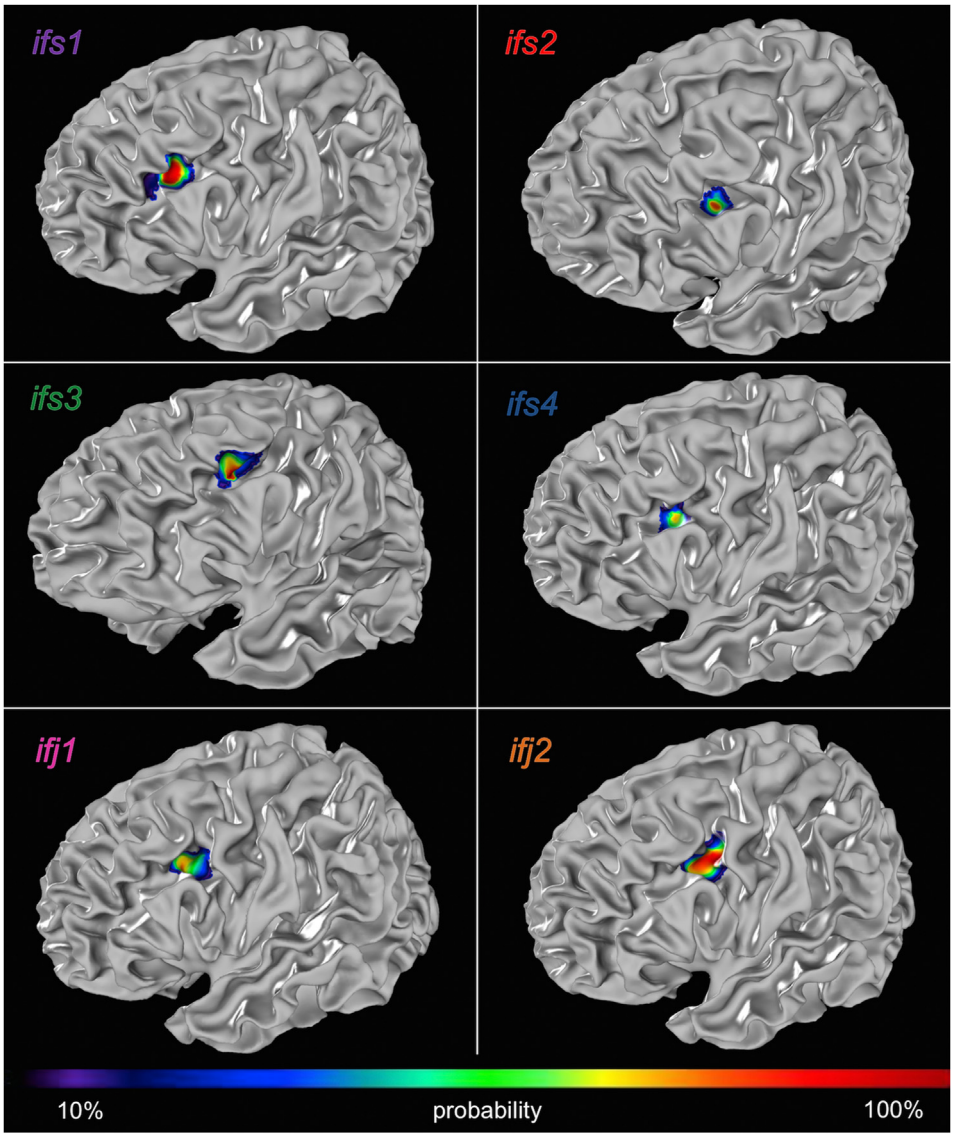


**Fig. 6 – Cytoarchitectonic probabilistic maps (pmaps) of *ifs*1-4, *ifj*1, and *ifj*2 of the left hemisphere. Each voxel indicates the frequency the area occurs in the stereotaxic MNI Colin 27 template brain. Violett colour means that an area is located in this voxel in only one of the mapped brains (10% probability), red that an area is located in this voxel in all 10 studied brains (100% probability). The pmaps of areas *ifs*1 *ifs*1 (DOI: https://www.doi.org/10.25493/HNZP-56M), *ifs*2 (DOI: https://www.doi.org/10.25493/NJD4-CM4), *ifs*3 (DOI: https://www.doi.org/10.25493/DGGC-X7Q), *ifs*4 (DOI: https://www.doi.org/10.25493/P3QK-2V6), *ifj*1 (DOI: https://www.doi.org/10.25493/V9PK-H82), and *ifj*2 (DOI: https://www.doi.org/10.25493/1WG8-WBE) of the left and right hemisphere are part of the Julich-Brain, https://jubrain.humanbrainproject.eu (Amunts et al., 2020) can be viewed in the interactive atlas on EBRAINS.**

co-activations of right *ifj*1 were detected in right IFS, right IFJ, right IFG, bilateral aMCC and MFG, whereas those of right *ifs*1-4 were found in bilateral IFS and IFG. Differences in the co-activation patterns between *ifs*1/2, *ifs*3, and *ifs*4 are shown in S2 Fig and S2 Table. Left *ifs*1/2 was more co-activated with bilateral aMCC, left IFG and right MFG as left *ifs*3 and *ifs*4. Left *ifs*3 showed specific co-activations in left IFJ, left *ifs*4 in bilateral SMA, left IFG, preCG, IPG, IPS, SPG, and STG. Right *ifs*1/2 was specifically co-activated with bilateral SMA, left preCG, IFG, IFJ, and right IFJ, whereas the specifics of right *ifs*3 were located in right IFS, and those of *ifs*4 in the left preCG, SMA, aMCC, and right IFG, and IFJ.

## 4. Discussion

This study has identified and characterized six new cortical areas, *ifs*1-*ifs*4, *ifj*1, and *ifj*2 within the IFS and IFJ based on differences in their cyto- and receptor architecture, thereby identifying a unique structurally and functionally distinct region in-between the mid-dorsolateral and ventrolateral prefrontal cortex. It builds upon and agrees with results of an earlier study addressing the receptor architecture of the extended Broca's region (Amunts et al., 2010). The multimodal analysis based on 17 receptor types of different

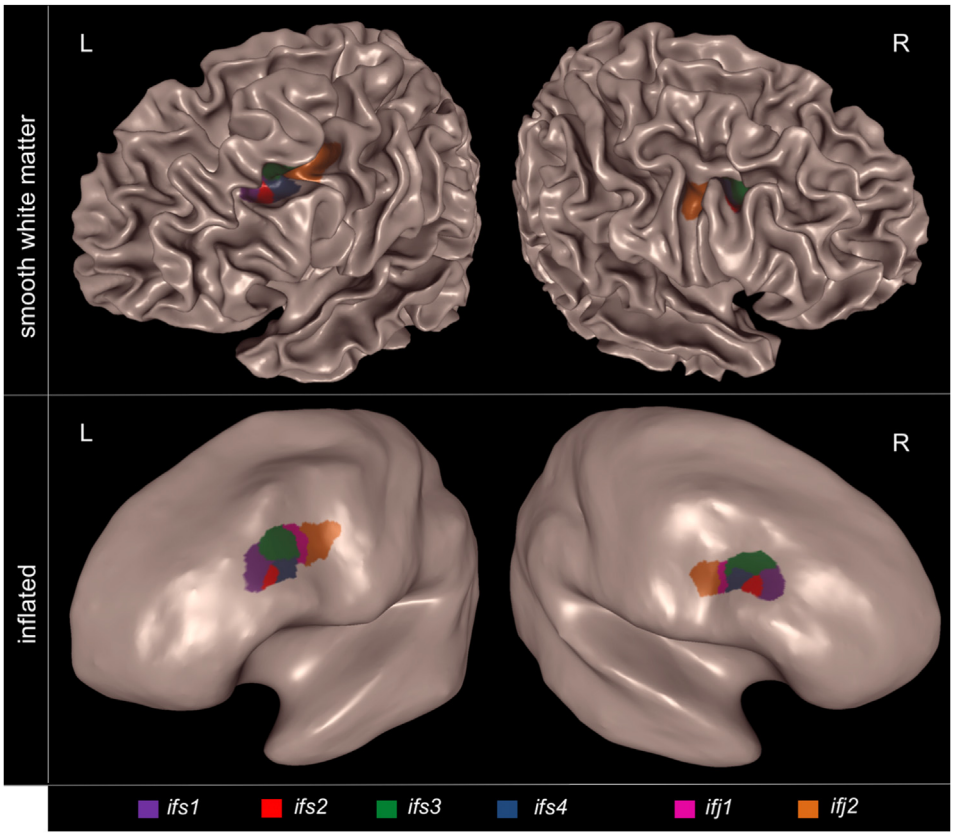


**Fig. 7 – Cytoarchitectonic maximum probability maps (MPM) of *ifs1-ifs4*, *ifj1* and *ifj2* of the left (L) and right hemisphere (R) in MNI-Colin27 template brain. The maps were calculated on basis of the pmaps and are presented in smooth white matter (top) and inflated mode (bottom) to visualize the areas in the depths of the sulci. The MPMs are part of the Julich-Brain https://jubrain.humanbrainproject.eu and integrated in the multilevel human brain Atlas on EBRAINS.**

**Table 1 – Coordinates of the centre of gravity of probabilistic maps (pmaps) of *ifs1-4*, *ifj1*, and *ifj2* of the left (L) and right (R) hemisphere in ICBM 2009c nonlinear asymmetric space.**

| area | hemisphere | x | y | z |
|---|---|---|---|---|
| *ifs1* | L | −40 | 27 | 22 |
| *ifs1* | R | 37 | 26 | 25 |
| *ifs2* | L | −44 | 25 | 22 |
| *ifs2* | R | 43 | 25 | 24 |
| *ifs3* | L | −42 | 20 | 29 |
| *ifs3* | R | 38 | 23 | 33 |
| *ifs4* | L | −44 | 19 | 24 |
| *ifs4* | R | 42 | 22 | 28 |
| *ifj1* | L | −40 | 14 | 29 |
| *ifj1* | R | 41 | 16 | 28 |
| *ifj2* | L | −42 | 8 | 30 |
| *ifj2* | R | 43 | 11 | 26 |

neurotransmitter systems showed that the new areas in the IFS and IFJ are highly similar between each other, but more distinct to dorsally and ventrally adjacent areas. The study therefore provides evidence that the prefrontal cortex shows an additional, third domain, which is distinct from areas of the dorso- and ventrolateral prefrontal cortex. Based on previous work, which showed that functionally related areas reveal similarities in receptor distribution patterns (Zilles & Amunts, 2009; Zilles et al., 2015), we may assume that this segregation has functional correlates.

Studies of other sulcus regions have also demonstrated the existence of distinct areas within sulci, for example, for the intraparietal sulcus (Choi et al., 2006; Richter et al., 2019; Scheperjans et al., 2008) and the superior temporal sulcus (Zachlod et al., 2020). A similar pattern seems to be present in the IFS and IFJ according to the findings of the present study, which indicates a more fine-grained parcellation than previously assumed. A distinction of sulcus areas from areas located on neighbouring gyri would be in line with the tension-based theory of cortical folding postulated by van Essen (Van Essen, 1997). This theory claims that early developed and highly interconnected areas were pulled towards one another by mechanical tension along axons during cerebral growth to shorten neuronal transmission distances. Thus, sulcus areas might be more strongly interconnected with each other and therefore more functional related than with areas located on the inferior and middle frontal gyri. The tension-based theory also offers an explanation why one of the *ifs* areas, *ifs3*, reaches in some cases the surface of the middle frontal gyrus whereas the *ifj* areas are restricted to the sulci. It was described that the association between sulcus morphology and sulcus areas is less consistent, the later the

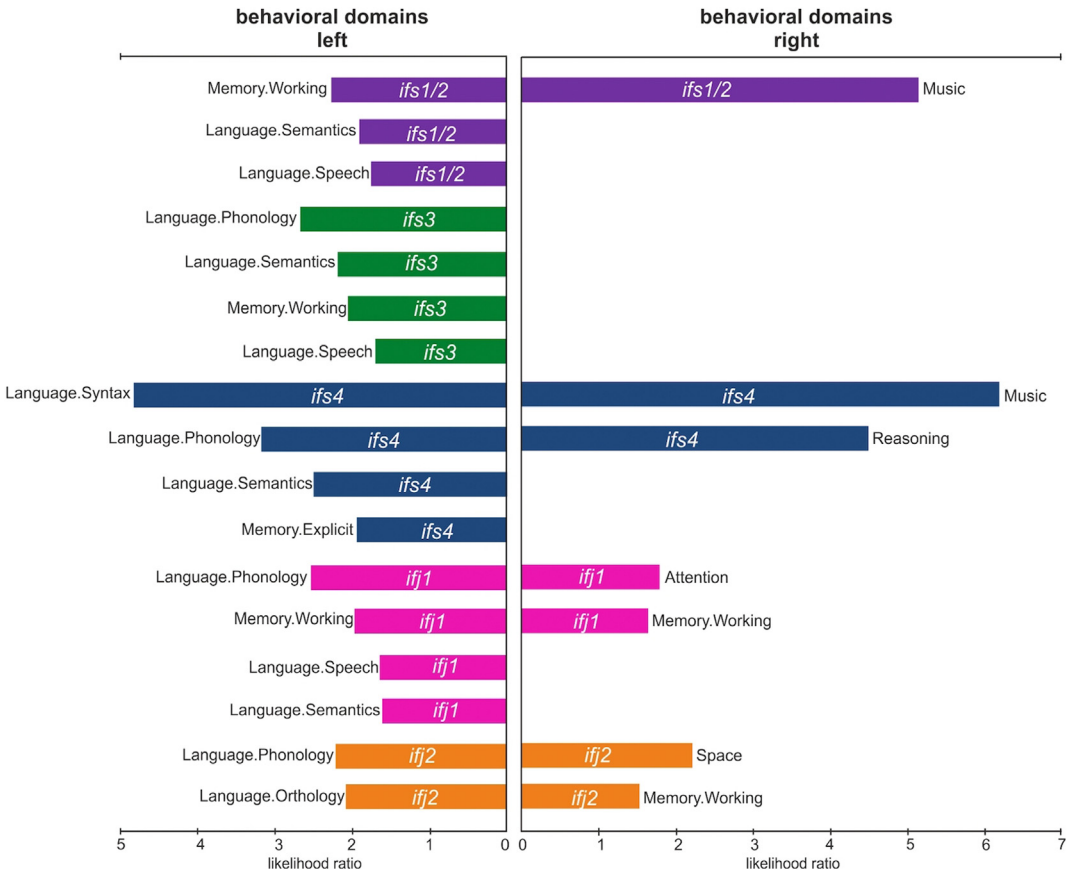


**Fig. 8 – Behavioral domains of cognition significantly associated with areas *ifs1/2*, *ifs3*, *ifs4*, *ifj1*, and *ifj2* of the left and right hemisphere. Left areas are involved in language processes and working memory, their right hemispheric correlates mainly in music processing, working memory, and attention. ($p < .05$, Bonferroni corrected for multiple comparisons).**

given sulcus develops. The IFS is a tertiary sulcus and appears relatively late, in the 30th week (Nishikuni & Ribas, 2013). In contrast, the primary somatosensory area 3 is exclusively located within the central sulcus (Geyer et al., 1999), which is one of the first sulci during ontogeny. Furthermore, the border between areas 44 and 45 in Broca's region is not consistently defined by the diagonal sulcus or any other sulcus (Amunts et al., 1999). The diagonal sulcus is appearing even later in the development (Nishikuni & Ribas, 2013). This might explain why *ifs3* reached out of the ontogenetic younger IFS on the free surface of the middle frontal gyrus.

The results of the hierarchical cluster analysis of the receptor densities revealing a functional distinction of the areas in the IFS. Miller et al. (2021a) have also shown that another tertiary sulcus in the prefrontal cortex, the middle frontal sulcus is subdivided into 3 distinct regions with an underestimated function in cognition. Since *ifs1*-*ifs4*, *ifj1*, and *ifj2* have been described in this study for the first time, their functions still have to be elucidated. Indications may come from functional imaging studies reporting distinct activation clusters within the IFS and IFJ. However, the new cortical areas are rather small and they show a high inter-individual variability in 3D space, also caused by the variability in the sulcal pattern of IFS and IFJ. As a result, activation clusters resulting from neuroimaging may cover more than one cytoarchitectonic map when superimposing both data. In addition, a cluster can also cover several cytoarchitectonic areas because the given task might be less specific to reveal an activation of only one area and requires the activity of several functionally related neighbouring areas. Still, several fMRI studies are instrumental to better understand the cognitive function of the new areas. Brass et al. (Brass & von Cramon, 2002) first described an IFJ activation in a study addressing cognitive control in a task switching paradigm. Building on this study, Derrfuss et al. (2009) analysed the inter-individual variability of this IFJ activation and its association with the sulcal pattern. The authors reported variable inter-individual peak coordinates which were caused by the high variability of preCS and IFS as well as their junction. That the sulcal pattern is highly variable and therefore causes variability in the location of the *ifs* and *ifj* areas was also shown by our study. Individual activation clusters showed that the cytoarchitectonic area underlying activations of the IFJ might be located in the inferior preCS dorsally and ventrally to the junction with the IFS, with an extension into the IFS. These findings are in accordance with the results of the present study. Areas *ifj1* and *ifj2* taken together show a similar localization and extent as the described IFJ activation. Therefore, it can be assumed that the performed task switching paradigm involved both *ifj1* and *ifj2* and that this IFJ activation consists of both areas, *ifj1* and *ifj2*. Such functional relationship of the *ifj* areas was reflected by the cluster analysis as well.

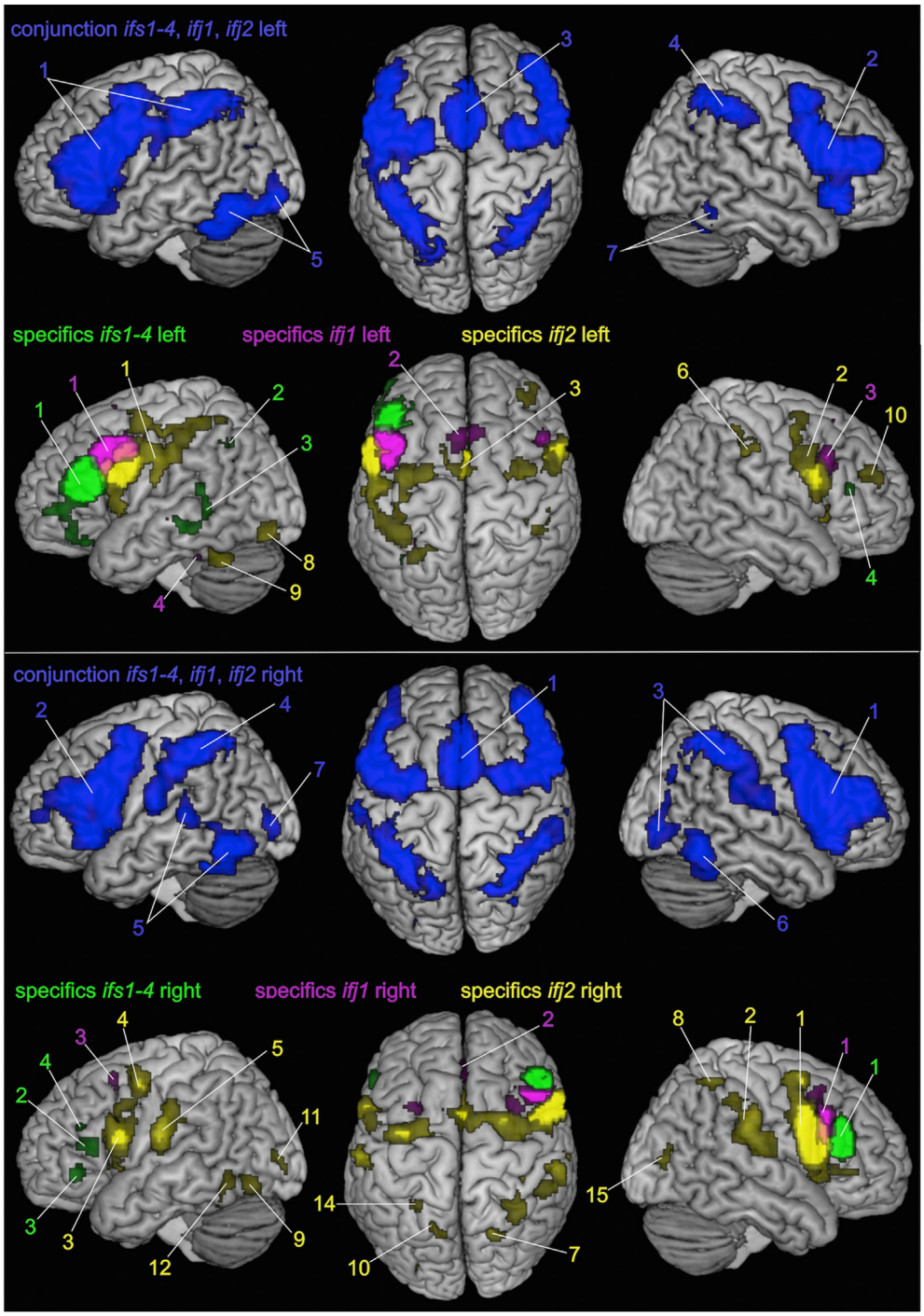


**Fig. 9 – Conjunctions across co-activations of *ifs*1-4, *ifj*1 and *ifj*2 (brain regions co-activated with all these areas) and specific co-activation patterns of *ifs*1-4, *ifj*1 and *ifj*2 (brain regions significantly more co-activated with the considered area than with the others) of the left and right hemisphere. Anatomical assignment of the co-activation clusters labelled with colour coded numbers are presented in Table 2. (cluster-level FWE corrected $p < .05$, cluster-forming threshold at voxel level $p < .001$).**

In a functional imaging study of Makuuchi et al. (2009) on verbal working memory, three activation clusters were found within the left IFS (LIFS): an anterior LIFS (LIFSa), a middle LIFS (LIFSm) and a posterior LIFS (LIFSp) cluster. These findings support the rosto-caudal organization of areas within the IFS as shown for *ifs*1-4, *ifj*1, and *ifj*2. Peak coordinates of these clusters were located within the pmaps of different *ifs* and *ifj* areas delineated in our study. The peak of LIFSa is located within the pmaps of *ifs*1 and *ifs*2, that of LIFSm within those of *ifs*3 and *ifs*4, and that of LIFSp within the pmaps of *ifj*1 and *ifj*2. These findings indicate that cluster LIFSa consists of the activation of both areas *ifs*1 and *ifs*2, LIFSm of *ifs*3 and *ifs*4, and LIFSp of *ifj*1 and *ifj*2. These close functional relationships of these areas were

**Table 2 – Anatomical assignment and cytoarchitectonic areas of the conjunction and specific co-activation clusters *ifs*1-4, *ifj*1 and *ifj*2 of the left and right hemisphere shown in Fig. 9. Cytoarchitectonic areas according to the Julich-Brain atlas.**

| cluster number | cluster size (voxel) | macroanatomical location | cytoarchitectonic areas | MNI coordinates x | y | z |
|---|---|---|---|---|---|---|
| **co-activations conjunction *ifs*1-4, *ifj*1, *ifj*2 left** | | | | | | |
| 1 | 11,412 | L IFS, L IFG | *ifs*1/2 (97%), *ifs*3 (88%), *ifs*4 (100%), 44[a] (48%), 45[a] (50%) | −44 | 46 | 19 |
| | | L IFJ, L preCG | *ifj*1 (96%), *ifj*2 (100%) | −46 | 4 | 32 |
| | | L FOP | | −51 | 13 | 1 |
| | | L LOG | | −46 | 21 | −3 |
| | | L preCG | | −28 | −4 | 54 |
| | | L IL | | −34 | 22 | 1 |
| | | L putamen | | −23 | −1 | 5 |
| | | L postCG | 1[l] (11%), 3b[l] (34%), 4p[k] (30%) | −52 | −23 | 40 |
| | | | | −59 | −18 | 27 |
| | | | | −38 | −27 | 52 |
| | | L IPG | PFt[c] (53%) | −42 | −42 | 46 |
| | | L IPS | hIP1[b] (49%), hIP2[b] (81%), hIP3[g] (100%) | −30 | −58 | 48 |
| | | L SPG | 7A[g] (37%), 7PC[g] (66%), 5L[g] (8%) | −26 | −63 | 47 |
| | | L SOG | | −25 | −74 | 41 |
| 2 | 5804 | R IFS, R IFG | *ifs*1/2 (46%), *ifs*3 (32%), *ifs*4 (98%), 44[a] (57%), 45[a] (34%) | 51 | 21 | 23 |
| | | R IFJ | ifj1 (100%), ifj2 (100%) | 51 | 9 | 29 |
| | | R FOP | | 50 | 15 | −4 |
| | | R MFG | | 43 | 37 | 23 |
| | | R preCG | | 33 | −2 | 55 |
| | | R IL | | 35 | 23 | −1 |
| | | R putamen | | 24 | 7 | 3 |
| | | R thalamus | | 11 | −16 | 7 |
| 3 | 3009 | L aMCC, L pMCC, | 32′[f] (70%), 24c′[f] (48%), a24a' & a24b′[f] (58%), p24a' & p24b′[f] (23%), 24dv, 24dd[f] (32%) | 1 | 16 | 44 |
| | | R aMCC, R pMCC, | 32′[f] (64%), 24c′[f] (56%), a24a' & a24b′[f] (50%), p24a' & p24b′[f] (16%), 24dv, 24dd[f] (38%) | | | |
| | | L SMA, R SMA | | 0 | 6 | 52 |
| 4 | 2084 | R IPG, R IPS | PFt[c] (15%), hIP1[b] (43%), hIP2[b] (72%), hIP3[g] (89%) | 40 | −46 | 45 |
| | | R AG, R SPG | 7A[g] (38%), 7PC[g] (21%) | 32 | −59 | 49 |
| | | R MOG | | 29 | −76 | 31 |
| 5 | 1671 | L FG | FG3[e] (42%), FG2[d] (64%) | −44 | −51 | −14 |
| | | | | −42 | −66 | −12 |
| | | L IOG | hOc4la[j] (21%), hOc4lp[j] (27%), hOc4v[i] (8%) | −38 | −86 | −10 |
| | | L MOG | | −26 | −93 | −4 |
| 6 | 574 | L thalamus | | −10 | −17 | 6 |
| 7 | 369 | R cerebellum | | 24 | −62 | −22 |
| | | R FG | FG3[e] (5%) | 44 | −56 | −20 |
| | | R ITG | | 47 | −58 | −10 |
| **specific co-activations *ifj*2 left** | | | | | | |
| 1 | 2985 | L IFJ, L IFG, L preCG | *ifj*2 (22%), 44[a] (42%) | −48 | 1 | 26 |
| | | L FOP | | −44 | 4 | 8 |
| | | L preCG | | −33 | −11 | 76 |
| | | L postCG | 3b[l] (28%), 4p[k] (30%), 1[l] (10%) | −38 | −29 | 52 |
| | | | | −51 | −16 | 40 |
| | | | | −59 | −18 | 26 |
| | | L SMG | PFt[c] (47%) | −50 | −33 | 40 |
| | | L IPG | | −49 | −37 | 51 |
| | | L IPS | hIP2[b] (22%) | 41 | −46 | 57 |
| 2 | 1159 | R IFJ, R IFG | *ifj*2 (73%), 44[a] (35%) | 58 | 7 | 25 |
| | | R preCG | | 48 | 0 | 28 |
| | | | | 34 | −7 | 62 |
| 3 | 1074 | L pMCC | 24dv, 24dd[f] (32%) | −4 | 4 | 44 |
| | | R pMCC | 24dv, 24dd[f] (37%) | 12 | 14 | 40 |
| | | L SMA, R SMA | | −2 | −4 | 53 |
| 4 | 280 | L putamen | | −28 | −2 | 4 |
| 5 | 269 | R putamen | | 30 | 12 | 2 |
| 6 | 255 | R SMG | PFt[c] (12%) | 50 | −36 | 40 |
| | | R IPG | | 42 | −40 | 56 |

(*continued on next page*)

**Table 2 – (*continued*)**

| cluster number | cluster size (voxel) | macroanatomical location | cytoarchitectonic areas | MNI coordinates x | y | z |
|---|---|---|---|---|---|---|
| 7 | 154 | L thalamus | | −13 | −21 | 8 |
| 8 | 130 | L IOG | hOc4lp[j] (6%), hOc4v[i] (5%) | −36 | −88 | −12 |
| 9 | 130 | L cerebellum | | −42 | −60 | −28 |
| 10 | 122 | L MFG | | 36 | 34 | 33 |
| 11 | 116 | R cerebellum | | 20 | −59 | −22 |
| 12 | 115 | R thalamus | | 13 | −18 | 8 |
| **specific co-activations *ifj1* left** | | | | | | |
| 1 | 873 | L IFJ, L IFG | *ifj1* (46%), *ifj2* (49%), 44[a] (6%) | −42 | 11 | 46 |
| 2 | 277 | L SMA, R SMA | | 0 | 15 | 57 |
| 3 | 123 | R IFS | *ifs3* (16%) | 48 | 14 | 38 |
| 4 | 87 | L FG | FG3[e] (4%), FG4[e] (5%) | −36 | −42 | −18 |
| **specific co-activations *ifs1-4* left** | | | | | | |
| 1 | 1871 | L IFS, L IFG | *ifs1/2* (100%), *ifs3* (88%), *ifs4* (94%) | −42 | 24 | 22 |
| | | L IFG | 45[a] (28%) | −42 | 40 | 5 |
| | | L LOG | | −43 | 32 | −8 |
| | | | | −40 | 25 | −16 |
| 2 | 160 | L IPS | hIP1[b] (26%), hIP3[g] (16%) | −34 | −62 | 46 |
| | | L AG | | −34 | −62 | 38 |
| | | | | −34 | 56 | 34 |
| 3 | 156 | L ITG | | −60 | −48 | 16 |
| | | L MTG | | −59 | −50 | 4 |
| | | | | −58 | −38 | −6 |
| 4 | 88 | R IFS | *ifs1/2* (18%) | 36 | 20 | 22 |
| | | | | 36 | 28 | 18 |
| **co-activations conjunction *ifs1-4*, *ifj1*, *ifj2* right** | | | | | | |
| 1 | 11,657 | R IFS, R IFG | *ifs1/2* (48%), *ifs3* (65%), *ifs4* (100%), 44[a] (47%), 45[a] (88%) | 50 | 25 | 25 |
| | | R IFJ, R preCG | *ifj1* (100%), *ifj2* (100%) | 48 | 8 | 28 |
| | | R FOP | | 51 | 15 | −2 |
| | | R preCG | | 30 | −3 | 57 |
| | | R MFG | | 44 | 38 | 22 |
| | | R IL | | 37 | 21 | 1 |
| | | R aMCC, R pMCC, | 32′[f] (77%), 24c′[f] (55%), a24a' & a24b′[f] (57%), p24a' & p24b′[f] (26%), 24dv, 24dd[f] (39%) | 0 | 8 | 52 |
| | | L aMCC, L pMCC | 32′[f] (66%), 24c′[f] (34%), a24a' & a24b′[f] (63%), p24a' & p24b′[f] (30%), 24dv, 24dd[f] (24%) | | | |
| | | R SMA, L SMA | | | | |
| | | R thalamus | | 12 | −15 | 7 |
| | | L thalamus | | −10 | −18 | 7 |
| | | R putamen | | 23 | 5 | 3 |
| | | R caudatus | | 14 | 6 | 9 |
| | | L caudatus | | −12 | −1 | 11 |
| 2 | 6194 | L IFS, L IFG | *ifs1/2* (76%), *ifs3* (63%), *ifs4* (100%), 44[a] (81%), 45[a] (23%) | −46 | 24 | 24 |
| | | L IFJ, L preCG | *ifj1* (68%), *ifj2* (100%) | −48 | 7 | 32 |
| | | L FOP | | −51 | 7 | 7 |
| | | L preCG | | −26 | −5 | 56 |
| | | L MFG | | −40 | 48 | 10 |
| | | L IL | | −33 | −13 | 2 |
| | | L putamen | | −21 | 1 | 4 |
| 3 | 3776 | R IPG, IPS | PFm[c] (18%), hIP1[b] (46%), hIP2[b] (89%), hIP3[g] (90%) | 34 | −52 | 48 |
| | | R SPG | 7A[g] (32%), 7PC[g] (32%), 7P[g] (12%) | 30 | −62 | 50 |
| | | R SMG | PFcm[c] (45%), PFop[c] (41%), PFt[c] (39%), PF[c] (30%) | 60 | −38 | 30 |
| | | | | 56 | −32 | 34 |
| | | R POP | OP1[h] (39%) | 63 | −23 | 21 |
| | | R SOG | | 32 | −75 | 36 |
| | | R MOG | hOc4lp[j] (33%) | 33 | −89 | 3 |
| 4 | 3205 | L IPS | hIP1[b] (31%), hIP2[b] (73%), hIP3[g] (92%) | −30 | −54 | 50 |
| | | L IPG | PFt[c] (55%) | −40 | −40 | 42 |
| | | L SPG | 7A[g] (43%), 7PC[g] (59%), 5L[g] (8%) | −16 | −66 | 56 |
| | | L SMG | PFop[c] (50%) | −56 | −22 | 20 |
| | | L POP | OP1[h] (43%) | | | |
| | | L postCG | 3b[l] (10%) | −40 | −29 | 53 |

**Table 2 – (*continued*)**

| cluster number | cluster size (voxel) | macroanatomical location | cytoarchitectonic areas | MNI coordinates x | y | z |
|---|---|---|---|---|---|---|
| 5 | 1292 | L STG | | −55 | −41 | 12 |
| | | L MTG | | −50 | −58 | 4 |
| | | L FG, L IOG | FG2[d] (53%), FG3[e] (53%), hOc4la (21%) | −45 | −64 | −11 |
| 6 | 1003 | R cerebellum | | 20 | −58 | −20 |
| | | R FG | FG3[e] (26%), FG2[d] (51%), FG1[d] (35%), FG4[e] (8%) | 45 | −62 | −14 |
| 7 | 220 | R MOG | hOc4lp[j] (19%) | −26 | −94 | 4 |
| | | | | −26 | −80 | 26 |
| **specific co-activations *ifj2* right** | | | | | | |
| 1 | 3777 | R IFJ, R IFG, R preCG | *ifj2* (80%), 44 (65%) | 51 | 4 | 28 |
| | | R preCG | | 29 | −4 | 58 |
| | | R FOP | | 58 | 6 | 10 |
| | | R IL | | | | |
| | | R IFG | | 49 | 27 | 5 |
| | | R pMCC, | p24a' & p24b'[f] (26%), 24dv, 24dd[f] (24%) | 5 | 10 | 36 |
| | | L pMCC | p24a' & p24b'[f] (25%) | | | |
| | | R SMA, L SMA | | 5 | 0 | 52 |
| | | R putamen | | 27 | 4 | 4 |
| 2 | 979 | R SMG | PFop[c] (40%), PFt[c] (30%), PFcm[c] (37%), PF[c] (24%), PFm[c] (8%) | 58 | −32 | 34 |
| | | R POP | OP1[h] (30%) | 60 | −24 | 21 |
| | | R IPS, R IPG | hIP2[b] (46%) | 42 | −36 | 44 |
| 3 | 701 | L IFG, L preCG | 44[a] (37%) | −56 | 4 | 21 |
| | | L FOP, L IL | | −41 | 5 | 7 |
| | | L preCG | | −54 | −2 | 42 |
| 4 | 589 | L preCG | | −33 | −8 | 53 |
| 5 | 529 | L SMG | PFop[c] (47%), PFt[c] (30%) | −56 | −26 | 36 |
| | | | | −60 | −21 | 26 |
| | | L POP | OP1[h] (47%) | −58 | −20 | 22 |
| 6 | 285 | L putamen | | −23 | −2 | 3 |
| 7 | 182 | R SPG | 7P[g] (10%), 7A[g] (6%) | 21 | −70 | 53 |
| 8 | 138 | R SPG | 7PC[g] (16%) | 36 | −56 | 60 |
| 9 | 135 | L IOG | hOc4la[j] (11%) | −42 | −78 | −8 |
| 10 | 96 | L precuneus | 7A[g] (7%) | −14 | −66 | 56 |
| 11 | 79 | L MOG | hOc4lp[j] (9%) | −25 | −94 | 6 |
| 12 | 74 | L ITG | | −50 | −63 | −5 |
| 13 | 55 | L thalamus | | −14 | −21 | 11 |
| 14 | 54 | L SPG | 5L[g] (3%), 7PC[g] (10%) | −26 | −54 | 56 |
| 15 | 53 | L MOG | hOc4lp[j] (3%) | 33 | −84 | 12 |
| **specific co-activations *ifj1* right** | | | | | | |
| 1 | 625 | R IFJ, R IFS, R IFG | *ifj1* (74%), *ifj2* (15%), *ifs3* (40%), *ifs4* (40%), 45[a] (5%) | 44 | 14 | 35 |
| | | R MFG | | 34 | 7 | 52 |
| 2 | 144 | R aMCC, | 32'[f] (19%) | 6 | 26 | 36 |
| | | L aMCC | 32'[f] (10%) | | | |
| 3 | 53 | L MFG | | −28 | 7 | 56 |
| **specific co-activations *ifs1-4* right** | | | | | | |
| 1 | 781 | R IFS, R IFG | *ifs1/2* (92%), *ifs3* (35%), *ifs4* (51%), 45[a] (12%) | 46 | 24 | 24 |
| 2 | 111 | L IFG | 45[a] (11%) | −53 | 22 | 16 |
| 3 | 82 | L IFG | | −43 | 30 | −1 |
| 4 | 53 | L IFS | *ifs1/2* (8%) | −33 | 24 | 22 |

[a] 44, 45 (Amunts et al., 1999); [b] hIP2, hIP1 (Choi et al., 2006); [c] PFop, PFt, PF, PFm, PFcm (Caspers et al., 2006), [d] FG1, FG2 (Caspers et al., 2013), [e] FG2, FG3 (Lorenz et al., 2017), [f] 32', 24c',a24a' & a24b', p24a' & p24b', 24dv, 24dd (Palomero-Gallagher et al., 2009), [g] hIP3, 5L, 7 PC, 7P, 7A (Scheperjans et al., 2008), [h] OP1 (Eickhoff et al., 2006), [i] hOC3v, hOC4v (Rottschy et al., 2007), [j] hOc4lp, hOc4la (Kujovic et al., 2013), [k] 4p (Geyer et al., 1996), [l] 1, 3b (Geyer et al., 1999). IFS, inferior frontal sulcus; IFJ, inferior frontal junction; IFG, inferior frontal gyrus; MFG, middle frontal gyrus; preCG, precentral gyrus, postCG, postcentral gyrus; FOP, frontal Operculum; POP, parietal Operculum; LOG, lateral orbital gyrus; aMCC, anterior midcingulate cortex; pMCC, posterior midcingulate cortex; SMA, supplementary motor area; IPG, inferior parietal gyrus; IPS, intraparietal sulcus; SMG, supramarginal gyrus; AG, angular gyrus; SPG, superior parietal gyrus; ITG, inferior temporal gyrus; MTG, middle temporal gyrus; STG, superior temporal gyrus; IOG, inferior occipital gyrus; FG, fusiform gyrus; MOG, middle occipital gyrus; SOG, superior occipital gyrus; IL, insula lobe.

also indicated by our hierarchical cluster analysis of the receptor densities.

The inter-individual variability of the areas in the IFS and IFJ was high in comparison to areas 44 and 45 of Broca's region (Amunts et al., 1999), but comparable to areas of the intraparietal sulcus (Choi et al., 2006; Richter et al., 2019; Scheperjans et al., 2008). The high variability of the pmaps of *ifj1* and *ifj2* may be driven by a highly variable sulcus pattern of the IFS, and the different patterns of the IFJ in the investigated brains. Also Grefkes et al. (2004) indicated a consistent co-localization of activation clusters in the depths of the postcentral and intraparietal sulci and showed that the variability of the activation coordinates was caused by the variations and variability of the given sulcus itself. Studies of Choi et al. (2006) and Scheperjans et al. (2008) who cytoarchitectonically mapped the intraparietal sulcus further support a strong association between areas within this sulcus and its morphology. This view is also supported by Miller et al. (2021a) who identified a high inter-individual variability of the middle frontal gyrus. The small size of areas may also increase this effect because the smaller the size of an area in a variable sulcus, the smaller the region of overlap in the reference space. It should be mentioned that the probability maps provided in our study cannot include all anatomical details of the individual maps, but they provide a first reference to identify the cortical area underlying an activation in functional imaging studies. For a deeper understanding of the functional role of areas within the depth of sulci, it is still necessary to identify the individual pattern of the respective sulcus because of the strong structural-functional relationship of sulcus areas (Derrfuss et al., 2009; Miller et al., 2021a). New technological developments for automated sulci identification, in contrast to time-consuming manual identification, will increase the attention and consideration of sulcal areas in imaging studies und will help to understand the relationship of individual sulcal patterns on cognitive abilities (Miller et al., 2021a, 2021b).

To get a broad overview of the functions *ifs1-ifs4*, *ifj1*, and *ifj2* are involved in, we performed a coordinate-based meta-analysis using the BrainMap database. The advantage of this method is that thousands of studies investigating different mental processes can be analysed simultaneously. Restrictions of this method are the spatial resolution of the reported activations with voxel sizes not higher than 2 $mm^3$ which does not achieve that of our mapping experiments and the inter-subject variability of activations is approximately 10 mm because of the inexactness of spatial normalization (Eickhoff et al., 2009). It thus cannot be excluded that activations are assigned to one of the *ifs* or *ifj* areas even though they are in fact located in surrounding areas. This becomes more likely the smaller the areas are. The functional decoding of *ifs1-4*, *ifj1* and *ifj2* revealed a left-hemispheric lateralization of language related functions and a right-hemispheric lateralization of music processing and attention. Inter-hemispheric differences were also found in the co-activation patterns. This functional lateralization was in accordance to the findings in cyto- and receptor architecture of *ifs1-4*, *ifj1* and *ifj2*. Interestingly, we observed that 30% of the left hemispheres and 0% of the right hemispheres of the cytoarchtectonically mapped brains showed an interrupted IFS with only a short connection of the IFS with the preCS. Ono et al. (1990), on the other hand, reported incidence rates of 28% of the right hemisphere and 8% of the left hemisphere. To verify these results a larger sample size is needed. Also the effect of the separated *ifs* and *ifj* areas on their function is subject of future investigations. In addition, we showed that receptors BZ, kainate, $M_3$, and $GABA_A$, and particularly 5-$HT_{1A}$ were predominantly higher concentrated in the right areas which is in line with the study by Amunts et al. (2010) who found inter-hemispheric differences in receptor densities of Broca's region and surrounding cortices. Higher 5-$HT_{1A}$ receptor densities in the superior, middle and inferior frontal gyri of the right hemisphere were also reported by Fink et al. (2009) using PET. These results are of clinical relevance because multiple lines of research have implicated the role of 5-$HT_{1A}$ receptors in major depressive disorder. Studies showed a reduced number and binding potential of this receptor (Savitz et al., 2009) and a right-hemispheric hyperactivity in patients linking to the results that the right hemisphere is more involved in fear and other negative emotions which may underlie the elevated stress and anxiety in depression (Hecht, 2010). A functional lateralization of language and music is in accordance with the known lateralization of language to the left hemisphere (Broca, 1861) and those of music processing to the right one (Koelsch et al., 2002). Left *ifs1-4*, *ifj1*, and *ifj2*, all involved in language-related processes, showed common co-activations with regions of the language network (Friederici, 2011; Friederici & Gierhan, 2013). The temporal regions of the language network were specifically co-activated with left *ifs1-4*, more precisely the STG with *ifs4*. Friederici et al. (Friederici, 2011) described a temporo-frontal network enabling complex syntactic processes. These findings support our data indicating an involvement of left *ifs4* in syntax. This assumption is further supported by the above-mentioned study of Makuuchi et al. (2009). The authors pointed out that only the middle LIFS (LIFSm) cluster was associated with syntactic verbal working memory which was associated with *ifs4* and the functionally related *ifs3*. Right hemispheric *ifs* areas were involved in music processes. Their co-activations were located in brain regions described to be part of the before mentioned language network (Friederici & Gierhan, 2013). These findings are in accordance with the results of Koelsch et al. (2002), who examined the neural correlates of music processing and their relationship to right frontal regions. They demonstrated a network relevant for music processing similar to this language network, suggested that the cortical language network is less domain-specific than previously thought, and that both hemispheres interact during the processing of language and music.

In addition, our results showed that right *ifs3* and *ifj1* were associated with the behavioral domain attention, which agrees with data from Corbetta and Shulmann (Corbetta & Shulman, 2002). The authors identified a bilateral dorsal and a right lateralized ventral network responsible for attention which included bilateral IFJ and right hemispheric IFS activations. Further evidence for an involvement of the IFJ, by functional activations in studies investigating attention reporting activations in right *ifj1* (Langner & Eickhoff, 2013; Tamber-Rosenau et al., 2018; Zhang et al., 2018).

A further function, which might be associated with the right inferior prefrontal cortex is the inhibition of action (Rubia et al.,

2003). We found several activations located in right *ifs* and *ifj* areas which were assigned to the behavioral domain action inhibition, but further analysis and testing for significance revealed that this function is not specific for these areas.

Bilateral involvement of *ifs* and *ifj* areas was also found in working memory. The co-activation patterns of these areas are in accordance with Rottschy et al. (2012), who described a bilateral working memory network consisting of 44, 45, insula lobe, premotor cortex, (pre-) SMA, IPS, SPG, MFG, FG, cerebellum, thalamus, putamen, and caudatus using a coordinate-based meta-analysis across 189 working memory experiments. Additionally, the authors postulated a left dominant bilateral working memory "core" network which included clusters located mainly in left *ifs1/2*, *ifj1*, right *ifj1* and *ifj2*, areas also found to be involved in working memory by the functional decoding performed in our study. Various studies showed activation clusters within IFJ involved in cognitive control, e.g., (Brass & von Cramon, 2002; Derrfuss et al., 2004; Derrfuss et al., 2009) which falls under the umbrella of the behavioral domain of working memory in our analysis. Cole & Schneider (2007) identified a cognitive control network which included left and right IFJ. Muhle-Karbe et al. (2016) delineated two clusters (IFJ and IFS) in the left hemisphere associated with cognitive control using a co-activation based parcellation. They showed that the IFJ cluster was associated with the selection and specification of task demands whereas the IFS cluster was associated with interference resolution and attention shifts. The coordinate-based meta-analysis demonstrated that the *ifs* and *ifj* areas are involved in functions, which were previously attributed to one of the adjacent functional regions, the ventrolateral prefrontal cortex involved in linguistic and musical functions and the mid-dorsolateral prefrontal cortex in working memory. Distinct activation clusters within the IFS and IFJ as well as our cluster analysis revealed that the *ifs* and *ifj* areas forming a new functionally distinct region within the prefrontal cortex.

The results of these functional neuroimaging studies coincide with results of our cluster analysis and functional meta-analysis indicating an involvement of the *ifs* and *ifj* areas primarily in functions which are specific for the ventrolateral cortex but also in those of the mid-dorsolateral prefrontal cortex. Our connectivity based meta-analysis showed that *ifs1*-4, *ifj1*, and *ifj2* are also part of the relevant networks. Strikingly, left and right *ifj2* showed stronger connectivity with most regions in the conjunction analyses than the other *ifs* and *ifj* areas did which might give evidence that *ifj2* plays a prominent role in functions like language processing and working memory and might act as a functional hub between these networks.

The areal maps provided by this study will help to assign activations in functional imaging studies to *ifs1*-4, *ifj1* and *ifj2*, to distinguish activations from middle and ventral prefrontal areas from each other, and to be instrumental to determine their specific roles. The maps of *ifs1*-4, *ifj1* and *ifj2* are publicly available in the Julich-Brain (Amunts et al., 2020) https://www.fz-juelich.de/inm/inm-1/EN/Forschung/JulichBrain/JulichBrain_Webtools/JulichBrain_Webtools_node.html and is part of the Human Brain Atlas of the Human Brain Project (HBP, https://www.humanbrainproject.eu/en/explore-the-brain/atlases/). The integration and spatial alignment of multilevel datasets in the Atlas will allow analyses of further characteristics of the areas, e.g., with respect to their structural connectivity by using the 1000BRAINS study data (Caspers et al., 2014) or by analysing in which cognitive functions the areas involved in by using the high-spatial resolution, multi-task, fMRI dataset of the Individual Brain Charting project (Pinho et al., 2020). To support studies analysing structure-functional relationships, the maps are included in the SPM Anatomy Toolbox (https://github.com/inm7/jubrain-anatomy-toolbox). In addition to the maps of *ifs1*-4, *ifj1* and *ifj2*, their laminar cell densities and densities of 17 receptors are part of the Human Brain Atlas of HBP to provide a comprehensive dataset for brain modelling and simulation, to contribute to a better understanding of the multi-level complexity of the human brain by understanding the dynamically interactive processes between the levels reaching from cells and molecules to microcircuits, functional networks and brain functions (Grillner, 1996). Bridging the levels is one of the biggest goals of the Human Brain Project to which this study is contributing to.

To summarize, we showed for the first time that the IFS and IFJ are subdivided into six cyto- and receptor architectonically distinct areas which constitute a unique functional distinct region playing a crucial role in cognitive functions of the lateral prefrontal cortex. These results will influence the concept of how and where in the prefrontal cortex executive and language functions are processed.

## Open practices

The study in this article earned an Open Data badge for transparent practices. Materials and data for the study are available: Receptor densities: *ifs1* (DOI: https://www.doi.org/10.25493/SHG2-7RS), *ifs2* (DOI: https://www.doi.org/10.25493/14M7-QJR), *ifs3* (DOI: https://www.doi.org/10.25493/Z5JN-J28), *ifs4* (DOI: https://www.doi.org/10.25493/YF9R-J87), *ifj1* (DOI: https://www.doi.org/10.25493/JS85-VQD), and *ifj2* (DOI: https://www.doi.org/10.25493/VN1A-Q2R).

Probabilistic maps: *ifs1* (DOI: https://www.doi.org/10.25493/HNZP-56M), *ifs2* (DOI: https://www.doi.org/10.25493/NJD4-CM4), *ifs3* (DOI: https://www.doi.org/10.25493/DGGC-X7Q), *ifs4* (DOI: https://www.doi.org/10.25493/P3QK-2V6), *ifj1* (DOI: https://www.doi.org/10.25493/V9PK-H82), and *ifj2* (DOI: https://www.doi.org/10.25493/1WG8-WBE).

Interpolated maps in one of the 10 individual cytoarchitectonic mapped brains, the BigBrain: *ifs1* (DOI: https://www.doi.org/10.25493/YM3R-9SP), *ifs2* (DOI: https://www.doi.org/10.25493/6RNA-WG4), *ifs3* (DOI: https://www.doi.org/10.25493/RNQP-F5U), *ifs4* (DOI: https://www.doi.org/10.25493/GX3R-2ET), *ifj1* (DOI: https://www.doi.org/10.25493/18S5-89W), and *ifj2* (DOI: https://www.doi.org/10.25493/Z6GM-61X).

## CRediT author statement

**Sabine Helene Ruland**: Conceptualization, Validation, Formal Analysis, Investigation, Data Curation, Methodology, Writing – Original draft, Writing – Review & Editing, Visualisation, Project Administration.

**Nicola Palomero-Gallagher**: Methodology, Validation, Investigation, Formal Analysis, Writing – Review & Editing.

**Felix Hoffsteadter**: Formal Analysis, Writing – Review & Editing, Data curation.

**Simon B. Eickhoff**: Resources, Writing – Review & Editing.

**Hartmut Mohlberg**: Software, Formal Analysis, Writing – Review & Editing.

**Katrin Amunts**: Conceptualization, Methodology, Validation, Supervision, Writing – Review & Editing, Resources, Funding acquisition, project administration.

## Declaration of competing interest

None.

## Acknowledgements

This study was supported by the German Federal Ministry of Education and Research (BMBF 01GW0771). The research leading to these results has received funding from the European Union's Horizon 2020 Research and Innovation Programme under Grant Agreement No. 945539 (HBP SGA3).

Furthermore, the authors thank K. Zilles for scientific discussion, A. Schleicher for statistical analysis support as well as M. Cremer, J. Teske-Bausch, S. Behuet and R. Hübbers for excellent technical assistance.

## Supplementary data

Supplementary data to this article can be found online at https://doi.org/10.1016/j.cortex.2022.03.019.

## REFERENCES

Amunts, K., Kedo, O., Kindler, M., Pieperhoff, P., Mohlberg, H., Shah, N. J., … Zilles, K. (2005). Cytoarchitectonic mapping of the human amygdala, hippocampal region and entorhinal cortex: Intersubject variability and probability maps. *Anatomy and Embryology (Berl), 210*(5–6), 343–352.

Amunts, K., Lenzen, M., Friederici, A. D., Schleicher, A., Morosan, P., Palomero-Gallagher, N., & Zilles, K. (2010). Broca's region: Novel organizational principles and multiple receptor mapping. *Plos Biology, 8*(9).

Amunts, K., Lepage, C., Borgeat, L., Mohlberg, H., Dickscheid, T., Rousseau, M. E., … Evans, A. C. (2013). BigBrain: An ultrahigh-resolution 3D human brain model. *Science, 340*(6139), 1472–1475.

Amunts, K., Mohlberg, H., Bludau, S., & Zilles, K. (2020). Julich-brain: A 3D probabilistic atlas of the human brain's cytoarchitecture. *Science, 369*(6506), 988–992.

Amunts, K., Schleicher, A., Burgel, U., Mohlberg, H., Uylings, H. B., & Zilles, K. (1999). Broca's region revisited: Cytoarchitecture and intersubject variability. *Journal of Comparative Neurology, 412*(2), 319–341.

Amunts, K., & Zilles, K. (2015). Architectonic mapping of the human brain beyond Brodmann. *Neuron, 88*(6), 1086–1107.

Brass, M., & von Cramon, D. Y. (2002). The role of the frontal cortex in task preparation. *Cerebral Cortex, 12*(9), 908–914.

Broca, P. (1861). Remarques sur le sige de la facult du langage articul, suivies d'une observation d'aphemie (Perte de la Parole) (English Translation by Y. Grodzinsky & K. Amunts in Broca's Region, pp. 291-304, Oxford University Press, Oxford, New York, 2006: Comments regarding the seat of the faculty of spoken language, followed by an observation of aphemia (loss of speech)). *Bulletins et Memoires de la Societe Anatomique de Paris, 36*, 330–357.

Brodmann, K. (1909). *Vergleichende Lokalisationslehre der Großhirnrinde*. Leipzig: Barth.

Caspers, S., Geyer, S., Schleicher, A., Mohlberg, H., Amunts, K., & Zilles, K. (2006). The human inferior parietal cortex: Cytoarchitectonic parcellation and interindividual variability. *Neuroimage, 33*(2), 430–448.

Caspers, J., Zilles, K., Eickhoff, S. B., Schleicher, A., Mohlberg, H., & Amunts, K. (2013). Cytoarchitectonical analysis and probabilistic mapping of two extrastriate areas of the human posterior fusiform gyrus. *Brain Structure & Function, 218*(2), 511–526.

Caspers, S., Moebus, S., Lux, S., Pundt, N., Schutz, H., Muhleisen, T. W., … Erbel, R., et al. (2014). Studying variability in human brain aging in a population-based German cohort-rationale and design of 1000BRAINS. *Frontiers in Aging Neuroscience, 6*, 149.

Choi, H. J., Zilles, K., Mohlberg, H., Schleicher, A., Fink, G. R., Armstrong, E., & Amunts, K. (2006). Cytoarchitectonic identification and probabilistic mapping of two distinct areas within the anterior ventral bank of the human intraparietal sulcus. *Journal of Comparative Neurology, 495*(1), 53–69.

Cole, M. W., & Schneider, W. (2007). The cognitive control network: Integrated cortical regions with dissociable functions. *Neuroimage, 37*(1), 343–360.

Corbetta, M., & Shulman, G. L. (2002). Control of goal-directed and stimulus-driven attention in the brain. *Nature Reviews. Neuroscience, 3*(3), 201–215.

Demanet, J., Liefooghe, B., Hartstra, E., Wenke, D., De Houwer, J., & Brass, M. (2016). There is more into 'doing' than 'knowing': The function of the right inferior frontal sulcus is specific for implementing versus memorising verbal instructions. *Neuroimage, 141*, 350–356.

Derrfuss, J., Brass, M., & von Cramon, D. Y. (2004). Cognitive control in the posterior frontolateral cortex: Evidence from common activations in task coordination, interference control, and working memory. *Neuroimage, 23*(2), 604–612.

Derrfuss, J., Brass, M., von Cramon, D. Y., Lohmann, G., & Amunts, K. (2009). Neural activations at the junction of the inferior frontal sulcus and the inferior precentral sulcus: Interindividual variability, reliability, and association with sulcal morphology. *Human Brain Mapping, 30*(1), 299–311.

Eickhoff, S. B., Amunts, K., Mohlberg, H., & Zilles, K. (2006). The human parietal operculum. II. Stereotaxic maps and correlation with functional imaging results. *Cerebral Cortex, 16*(2), 268–279.

Eickhoff, S. B., Bzdok, D., Laird, A. R., Kurth, F., & Fox, P. T. (2012). Activation likelihood estimation meta-analysis revisited. *Neuroimage, 59*(3), 2349–2361.

Eickhoff, S. B., Laird, A. R., Grefkes, C., Wang, L. E., Zilles, K., & Fox, P. T. (2009). Coordinate-based activation likelihood estimation meta-analysis of neuroimaging data: A random-effects approach based on empirical estimates of spatial uncertainty. *Human Brain Mapping, 30*(9), 2907–2926.

Eickhoff, S. B., Stephan, K. E., Mohlberg, H., Grefkes, C., Fink, G. R., Amunts, K., & Zilles, K. (2005). A new SPM toolbox for combining probabilistic cytoarchitectonic maps and functional imaging data. *Neuroimage, 25*(4), 1325–1335.

Evans, A. C., Collins, D. L., Mills, S. R., Brown, E. D., & Kelly, R. L. (Eds.). (1993). *3D statistical neuroanatomical models from 305 MRI volumes*. New York, NY: IEEE.

Fink, M., Wadsak, W., Savli, M., Stein, P., Moser, U., Hahn, A., … Lanzenberger, R. (2009). Lateralization of the serotonin-1A receptor distribution in language areas revealed by PET. *Neuroimage, 45*(2), 598–605.
Fox, P. T., & Lancaster, J. L. (2002). Opinion: Mapping context and content: The BrainMap model. *Nature Reviews. Neuroscience, 3*(4), 319–321.
Friederici, A. D. (2011). The brain basis of language processing: From structure to function. *Physiological Reviews, 91*(4), 1357–1392.
Friederici, A. D., & Gierhan, S. M. (2013). The language network. *Current Opinion in Neurobiology, 23*(2), 250–254.
Geyer, S., Ledberg, A., Schleicher, A., Kinomura, S., Schormann, T., Burgel, U., … Roland, P. E. (1996). Two different areas within the primary motor cortex of man. *Nature, 382*(6594), 805–807.
Geyer, S., Schleicher, A., & Zilles, K. (1999). Areas 3a, 3b, and 1 of human primary somatosensory cortex. *Neuroimage, 10*(1), 63–83.
Grefkes, C., Ritzl, A., Zilles, K., & Fink, G. R. (2004). Human medial intraparietal cortex subserves visuomotor coordinate transformation. *Neuroimage, 23*(4), 1494–1506.
Grillner, S. (1996). From ion channels to networks and behavior: Modeling and biological experiments in interaction. *Neuroimage, 4*(3 Pt 2), S19–S22.
Hecht, D. (2010). Depression and the hyperactive right-hemisphere. *Neuroscience Research, 68*(2), 77–87.
Koelsch, S., Gunter, T. C., v Cramon, D. Y., Zysset, S., Lohmann, G., & Friederici, A. D. (2002). Bach speaks: A cortical "language-network" serves the processing of music. *Neuroimage, 17*(2), 956–966.
Kujovic, M., Zilles, K., Malikovic, A., Schleicher, A., Mohlberg, H., Rottschy, C., … Amunts, K. (2013). Cytoarchitectonic mapping of the human dorsal extrastriate cortex. *Brain Structure & Function, 218*(1), 157–172.
Laird, A. R., Eickhoff, S. B., Fox, P. M., Uecker, A. M., Ray, K. L., Saenz, J. J., Jr., … Fox, P. T. (2011). The BrainMap strategy for standardization, sharing, and meta-analysis of neuroimaging data. *BMC Research Notes, 4*, 349.
Laird, A. R., Eickhoff, S. B., Kurth, F., Fox, P. M., Uecker, A. M., Turner, J. A., et al. (2009). ALE meta-analysis workflows via the brainmap database: Progress towards A probabilistic functional brain atlas. *Frontiers in Neuroinformatics, 3*, 23.
Langner, R., & Eickhoff, S. B. (2013). Sustaining attention to simple tasks: A meta-analytic review of the neural mechanisms of vigilant attention. *Psychological Bulletin, 139*(4), 870–900.
Lorenz, S., Weiner, K. S., Caspers, J., Mohlberg, H., Schleicher, A., Bludau, S., … Amunts, K. (2017). Two new cytoarchitectonic areas on the human mid-fusiform gyrus. *Cerebral Cortex, 27*(1), 373–385.
Makuuchi, M., Bahlmann, J., Anwander, A., & Friederici, A. D. (2009). Segregating the core computational faculty of human language from working memory. *Proceedings of the National Academy of Sciences of the United States of America, 106*(20), 8362–8367.
Merker, B. (1983). Silver staining of cell bodies by means of physical development. *Journal of Neuroscience Methods, 9*(3), 235–241.
Miller, J. A., D'Esposito, M., & Weiner, K. S. (2021). Using tertiary sulci to map the "cognitive globe" of prefrontal cortex. *Journal of Cognitive Neuroscience*, 1–18.
Miller, J. A., Voorhies, W. I., Lurie, D. J., D'Esposito, M., & Weiner, K. S. (2021). Overlooked tertiary sulci serve as a meso-scale link between microstructural and functional properties of human lateral prefrontal cortex. *The Journal of Neuroscience: the Official Journal of the Society for Neuroscience, 41*(10), 2229–2244.
Muhle-Karbe, P. S., Derrfuss, J., Lynn, M. T., Neubert, F. X., Fox, P. T., Brass, M., & Eickhoff, S. B. (2016). Co-Activation-Based parcellation of the lateral prefrontal cortex delineates the inferior frontal junction area. *Cerebral Cortex, 26*(5), 2225–2241.
Nishikuni, K., & Ribas, G. C. (2013). Study of fetal and postnatal morphological development of the brain sulci. *Journal of Neurosurgery. Pediatrics, 11*(1), 1–11.
Ono, M., Kubik, S., & Abernathey, C. D. (1990). *Atlas of the cerebral sulci*. Stuttgart, New York: Thieme.
Palomero-Gallagher, N., Mohlberg, H., Zilles, K., & Vogt, B. (2008). Cytology and receptor architecture of human anterior cingulate cortex. *Journal of Comparative Neurology, 508*(6), 906–926.
Palomero-Gallagher, N., Vogt, B. A., Schleicher, A., Mayberg, H. S., & Zilles, K. (2009). Receptor architecture of human cingulate cortex: Evaluation of the four-region neurobiological model. *Human Brain Mapping, 30*(8), 2336–2355.
Petrides, M. (2000). The role of the mid-dorsolateral prefrontal cortex in working memory. *Experimental Brain Research, 133*(1), 44–54.
Pinho, A. L., Amadon, A., Gauthier, B., Clairis, N., Knops, A., Genon, S., … Double, C., et al. (2020). Individual Brain Charting dataset extension, second release of high-resolution fMRI data for cognitive mapping. *Scientific Data, 7*(1), 353.
Rajkowska, G., & Goldman-Rakic, P. S. (1995a). Cytoarchitectonic definition of prefrontal areas in the normal human cortex: I. Remapping of areas 9 and 46 using quantitative criteria. *Cerebral Cortex, 5*(4), 307–322.
Rajkowska, G., & Goldman-Rakic, P. S. (1995b). Cytoarchitectonic definition of prefrontal areas in the normal human cortex: II. Variability in locations of areas 9 and 46 and relationship to the talairach coordinate system. *Cerebral Cortex, 5*(4), 323–337.
Richter, M., Amunts, K., Mohlberg, H., Bludau, S., Eickhoff, S. B., Zilles, K., & Caspers, S. (2019). Cytoarchitectonic segregation of human posterior intraparietal and adjacent parieto-occipital sulcus and its relation to visuomotor and cognitive functions. *Cerebral Cortex, 29*(3), 1305–1327.
Rottschy, C., Eickhoff, S. B., Schleicher, A., Mohlberg, H., Kujovic, M., Zilles, K., & Amunts, K. (2007). Ventral visual cortex in humans: Cytoarchitectonic mapping of two extrastriate areas. *Human Brain Mapping, 28*(10), 1045–1059.
Rottschy, C., Langner, R., Dogan, I., Reetz, K., Laird, A. R., Schulz, J. B., … Eickhoff, S. B. (2012). Modelling neural correlates of working memory: A coordinate-based meta-analysis. *Neuroimage, 60*(1), 830–846.
Rousseeuw, P. (1987). Silhouettes: A graphical aid to the interpretation and validation of cluster analysis. *Journal of Computational and Applied Mathematics, 20*, 53–65.
Rubia, K., Smith, A. B., Brammer, M. J., & Taylor, E. (2003). Right inferior prefrontal cortex mediates response inhibition while mesial prefrontal cortex is responsible for error detection. *Neuroimage, 20*(1), 351–358.
Savitz, J., Lucki, I., & Drevets, W. C. (2009). 5-HT(1A) receptor function in major depressive disorder. *Progress in Neurobiology, 88*(1), 17–31.
Scheperjans, F., Hermann, K., Eickhoff, S. B., Amunts, K., Schleicher, A., & Zilles, K. (2008). Observer-independent cytoarchitectonic mapping of the human superior parietal cortex. *Cerebral Cortex, 18*(4), 846–867.
Schleicher, A., Amunts, K., Geyer, S., Kowalski, T., Schormann, T., Palomero-Gallagher, N., & Zilles, K. (2000). A stereological approach to human cortical architecture: Identification and delineation of cortical areas. *Journal of Chemical Neuroanatomy, 20*(1), 31–47.
Schleicher, A., & Zilles, K. (1990). A quantitative approach to cytoarchitectonics: analysis of structural inhomogeneities in nervous tissue using an image analyser. *Journal of Microscopy, 157*(3), 367–381.
Tamber-Rosenau, B. J., Asplund, C. L., & Marois, R. (2018). Functional dissociation of the inferior frontal junction from

the dorsal attention network in top-down attentional control. *Journal of Neurophysiology, 120*(5), 2498–2512.

Van Essen, D. C. (1997). A tension-based theory of morphogenesis and compact wiring in the central nervous system. *Nature, 385*(6614), 313–318.

Zachlod, D., Ruttgers, B., Bludau, S., Mohlberg, H., Langner, R., Zilles, K., & Amunts, K. (2020). Four new cytoarchitectonic areas surrounding the primary and early auditory cortex in human brains. *Cortex; a Journal Devoted To the Study of the Nervous System and Behavior, 128*, 1–21.

Zhang, X., Mlynaryk, N., Ahmed, S., Japee, S., & Ungerleider, L. G. (2018). The role of inferior frontal junction in controlling the spatially global effect of feature-based attention in human visual areas. *Plos Biology, 16*(6), Article e2005399.

Zilles, K., & Amunts, K. (2009). Receptor mapping: Architecture of the human cerebral cortex. *Current Opinion in Neurology, 22*(4), 331–339.

Zilles, K., Bacha-Trams, M., Palomero-Gallagher, N., Amunts, K., & Friederici, A. D. (2015). Common molecular basis of the sentence comprehension network revealed by neurotransmitter receptor fingerprints. *Cortex; a Journal Devoted To the Study of the Nervous System and Behavior, 63*, 79–89.

Zilles, K., Palomero-Gallagher, N., Grefkes, C., Scheperjans, F., Boy, C., Amunts, K., & Schleicher, S. (2002). Architectonics of the human cerebral cortex and transmitter receptor fingerprints: Reconciling functional neuroanatomy and neurochemistry. *European Neuropsychopharmacology: the Journal of the European College of Neuropsychopharmacology, 12*(6), 587–599.

Zilles, K., Schleicher, A., Palomero-Gallagher, N., & Amunts, K. (2002). Quantitative analysis of cyto- and receptor architecture of the human brain. In J. C. Mazziotta, & A. Toga (Eds.), *Brain mapping: The methods* (pp. 573–602). Amsterdam: Elsevier.